2019-08-01

Predicting Hardness of Friction Stir Processed 304L Stainless Steel using a Finite Element Model and a Random Forest Algorithm

Tyler Alan Mathis
Brigham Young University

Predicting Hardness of Friction Stir Processed 304L Stainless Steel Using a Finite Element Model and a Random Forest Algorithm

Tyler Alan Mathis

A thesis submitted to the faculty of
Brigham Young University
in partial fulfillment of the requirements for the degree of

Master of Science

Michael P. Miles, Chair
Tracy W. Nelson
David T. Fullwood

Department of Mechanical Engineering

Brigham Young University

ABSTRACT

Predicting Hardness of Friction Stir Processed 304L
Stainless Steel Using a Finite Element Model
and a Random Forest Algorithm

Tyler Alan Mathis
Department of Mechanical Engineering, BYU
Master of Science

Friction stir welding is an advanced welding process that is being investigated for use in many different industries. One area that has been investigated for its application is in healing critical nuclear reactor components that are developing cracks. However, friction stir welding is a complicated process and it is difficult to predict what the final properties of a set of welding parameters will be. This thesis sets forth a method using finite element analysis and a random forest model to accurately predict hardness in the welding nugget after processing. The finite element analysis code used and ALE formulation that enabled an Eulerian approach to modeling. Hardness is used as the property to estimate because of its relationship to tensile strength and grain size. The input parameters to the random forest model are temperature, cooling rate, strain rate, and RPM. Two welding parameter sets were used to train the model. The method was found to have a high level of accuracy as measured by R^2, but had greater difficulty in predicting the parameter set with higher RPM.

Keywords: friction stir welding, finite element analysis, grain size, hardness, machine learning, random forest

ACKNOWLEDGMENTS

I am grateful for many people who have made it possible for me to finish this thesis. Firstly, I would like to thank my committee chair, Doctor Miles, for taking me on as a research assistant and mentoring me through the process of writing a thesis. I would like to thank my other committee members, Doctor Nelson and Doctor Fullwood, for giving me guidance and expertise needed to complete this project.

I am grateful for the support of other students who have mentored me and whose research I have built on. Namely, Cameron Gunter, Cameron Gygi, Jeff Cramer, and Fengchao Liu.

I would like to thank Centre de Mise en Forme des Materiaux (CEMEF) for providing me with the research code to create the simulations.

Lastly, but most importantly, I would like to thank my wife and children for all their steady and consistent encouragement and support. All I have accomplished, I owe to them.

This work was supported by the National Science Foundation grant CMMI-1405508. Any opinions, findings, and conclusions or recommendations expressed in this material are those of the author and do not necessarity reflict the views of the National Science Foundation.

TABLE OF CONTENTS

LIST OF TABLES

LIST OF FIGURES

NOMENCLATURE

RPM	Revolutions per minute
FSW	Friction stir welding
FSP	Friction stir processing
FEA	Finite element analysis
SS	Stainless steel
SCC	Stress corrosion cracking
$TMAZ$	Thermo-mechanically affected Zone
HAZ	Head affected zone
$PCBN$	Polycrystalline cubic boron nitride
$FSSW$	Friction stir spot welding
CFD	Computational fluid dynamics
ALE	Arbitrary Lagrangian-Eulerian
ANN	Artificial neural network
FEM	Finite element model
MSE	Mean squared error
HV	Vickers Hardness
$\dot{\varepsilon}$	Strain rate
T	Temperature
$\dot{T}$	Cooling rate
Q	Activation energy

CHAPTER 1. INTRODUCTION

1.1 Overview

Friction stir welding (FSW) was first invented in 1991 by The Welding Institute (TWI) located in Cambridge, England [1]. FSW is used to join two metal substrates together similar to traditional fusion welding. FSW generally creates superior welds to fusion welding, but it has the drawback of requiring significant tooling to do so.

With the discovery that FSW can improve material properties, friction stir processing (FSP) was invented. FSP is effectively the same as FSW except its purpose is not to join plates together, but to improve the material properties of a plate by locally modifying microstructure and material properties.

In the current thesis, a finite element analysis (FEA) simulation is used to predict temperatures and strain rates for two set of FSP parameters. The temperatures and strain rates are then used to predict hardness, which is correlated to grain size, using a machine learning algorithm called random forest. The random forest algorithm is compared to the experimental hardness and an empirical equation to measure the accuracy of the model. The material used is 304L stainless steel (SS).

1.1.1 Motivation

One potential use of FSP applies to nuclear reactor components. Nuclear reactors in the United States are in need of repair due to the formation of surface cracks in SS components of the reactors. Irradiation from the cores causes a reaction with the nickel and boron in the steel that results in the formation of intergranular helium. Over time the heat from the cores causes the helium to aggregate eventually becoming surface cracks. One such component is the core shroud that is essential to running the reactors. If the surface cracks on the core shrouds develop into

through cracks, then the reactors will be shut down. FSP could be a possible method to repairing these cracks by processing over them to fill them in.

The repair of the nuclear reactors is critical because the power they generate constitutes a sizable amount of the total energy generated within the United States. In 2016, 19.7% of the total power generated within the United States was from nuclear reactors [2]. A major energy shortage could occur if the operation of these facilities was halted, which would cause energy costs to increase dramatically. Therefore, to prevent nuclear plant downtime, it is necessary to develop a repair method for the shrouds to extend the life of the current nuclear reactor fleet.

1.1.2 Current Repair Methods

The current method to repair surface cracks on the core shrouds is to attach large metal plates over the cracks. This method has proven effective at delaying more permanent repair methods. However, the shroud components will eventually either need to be replaced or be repaired with a more permanent solution.

One repair method that has been investigated is fusion welding. Unfortunately, this proposed repair method causes high temperatures, which has two negative consequences:

1. High temperatures will facilitate the development of malignant, chromium-dense phases to form, which will leave the rest of the stainless steel vulnerable to oxidation. This is because chromium is the material that protects stainless steel from destructive oxidation. If all of the chromium is grouped in one place, the rest of the steel matrix will be unprotected from oxidation.

2. High temperatures will promote dispersed helium atoms, created from neutron and alpha interactions, to aggregate, nucleating nanoscale bubbles. These bubbles will then coalesce and form intergranular cracks, accelerating crack propagation [3–5].

1.1.3 Proposed Repair Method

The proposed method of repair is to use FSP to process and repair the cracked material. The process will probably include fitting a 304L SS insert into the current cracks and processing

over the inserts. The temperatures caused by FSP are much lower than those caused by fusion welding which may reduce diffusion of helium bubbles and, in effect, intergranular cracking. FSP has also been shown to improve material properties in the weld nugget.

Even with lower operating temperatures, FSP may still cause harmful, chromium-rich phases to form which would negatively affect corrosion resistance. However, Gunter demonstrated that samples of 304L SS that had been processed at several different parameter sets did not oxidize after spending 1,000 hours in a room temperature corrosion tester in which the samples were repeatedly immersed in salt water and taken out [6]. It is not fully understood how these malignant phases form, however it is believed that their formation is correlated with recrystallization fraction. This thesis operates under the assumption that malignant phase formation can be correlated with recrystallization fraction. Creating an analytic method to predict final properties will accelerate the investigation of which FSP parameters will be most suitable for this application.

1.2 Machine Learning

Empirical models are generally used to predict properties after FSW; however, some authors are starting to investigate machine learning as another alternative to predicting properties. The advantage of machine learning is the ability of the algorithm to describe very complex relationships between variables. This is especially needed in FSW where these relationships are highly nonlinear. However, with many machine learning algorithms, overfitting is very easy which makes it difficult to tune the machine learning parameters to effectively predict properties without having bias.

1.3 Purpose Statement

The purpose of this study is to predict hardness in 304L SS after FSP. If hardness can be predicted, then resulting structural properties and the approximate amount of malignant, chromium-rich phase formation may be able to be predicted. The variables to predict hardness will be temperature, cooling rate, strain rate, and RPM.

1.4 Hypotheses

Hypothesis 1: The temperature of FSP can be estimated with an acceptable level of accuracy in the weld nugget using an FEA simulation.

Hypothesis 2: Final hardness can be predicted as a function of temperature, cooling rate, strain rate, and RPM using machine learning.

1.5 Delimitations

- The material in this study will be 304L SS and will not include any other materials.
- The only parameter sets that will be used in this thesis are 250 RPM, 100 mm/minute; and 80 RPM, 50 mm/minute where RPM is rotational velocity and mm/minute is translational velocity.

1.6 Significance of Study

The eventual goal of simulations should be to improve accuracy to match the value of physical experiments. Currently, authors who create and discuss simulations generally create those simulations using empirical equations to predict temperature, strain rate, and material flow for FSW. Very few are making the next step to predict additional material properties such as grain size and yield strength using machine learning. This thesis goes further than current authors by using processing results from an FEA simulation of FSP to predict hardness which is highly correlated to grain size and yield strength.

CHAPTER 2. LITERATURE REVIEW

2.1 304L Stainless Steel

Austenitic 304L SS is used frequently in harsh environments due to its superior corrosion resistance which comes from high chromium levels. Many nuclear reactors use 304L SS in environments where the steel is exposed to neutron irradiation because of its high capacity for neutron absorption. This absorption is due to its high nickel content and its boron content which is added to the 304L SS used in nuclear applications [7]. The composition of 304L SS used in this thesis can be viewed in table 2.1. The high corrosion resistance and large neutron absorption capacity makes this alloy ideal for nuclear applications.

Table 2.1: Composition of 304L stainless steel.

	C	Si	Mn	P	S	Cr	Ni	N	Fe
wt %	0.03	0.75	2.00	0.045	0.030	18.00/20.00	8.00/12.00	0.10	Balance

2.1.1 Stress Corrosion Cracking

Stress corrosion cracking (SCC) occurs when a metal develops cracks from the effects of being in a corrosive environment. Often, SCC can lead to sudden and catastrophic failure. In this thesis, the corrosive environment is composed of neutron bombardment of stainless steel components, elevated temperature in the reactor core, and parts submerged in water.

Neutrons radiating from the cores react with the nickel and boron in stainless steel forming helium. Over time, the helium atoms aggregate into intergranular cracks. This aggregation is accelerated by elevated temperatures in the nuclear reactors. Eventually, These intergranular cracks become substantial enough to become surface cracks and pose a danger to the reactor's function. It was found in irradiated 316 SS, a similar alloy to 304L SS, that even at very low levels of helium

concentration can lead to catastrophic cracking while fusion welding [8]. Asano et al found that there was a direct correlation between cracking and both heat and helium content while fusion welding irradiated stain [9].

2.2 Friction Stir Welding / Friction Stir Processing

FSW is used to join two plates together by plunging the rotating tool tip into the plate interface which then plasticizes the metal at the interface due to the friction generated by the rotating tool. Then the tool traverses across the weld, essentially mixing the two plates together. As the tool transverses across the weld, heat is generated by plastic deformation of the material. A diagram of the process is shown in figure 2.1 [10].

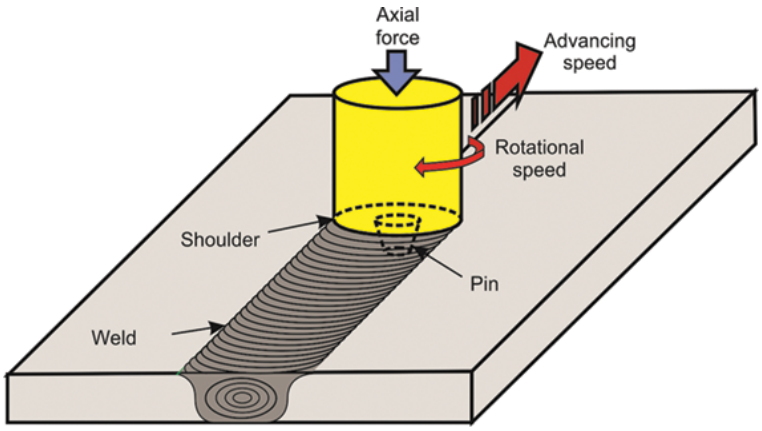

Figure 2.1: Diagram of friction stir welding.

There are many advantages of FSW over traditional welding methods. One major advantage is that there are many materials that are difficult to weld using fusion welding that can be welded using FSW, such as aluminum [11–15]. It can also easily join dissimilar metals [16]. FSW can create welds below the melting point which is useful to avoid forming undesirable phases and to improve material properties. FSW creates a microstructure that is far superior to that of fusion welding by forming small, equiaxed grains in the weld nugget [17–19]. These grains results in superplasticity in the weld nugget [12, 16, 20, 21]. FSW is also considered a ”green” process because of the lack of shielding gas needed to create the weld.

First used by Mishra et al, FSP is a slightly modified version of FSW in which, instead of joining two plates, friction stirring is used to process a line of metal to change its material properties [15]. FSP is used to reduce residual stresses, induce superplasticity, and improve strength. This superplasticity occurs from the Hall-Petch relation because the extreme plastic deformation transforms the base material grains in the weld nugget into very fine grains.

Mishra et al first investigated the superplasticity that develops in the weld nugget of aluminum alloys [15, 22]. Mahoney and Lynch investigated FSP in a number of materials and the improvement in material properties. They found that FSP doubles the strength of cast nickel-aluminum-bronze, increases the ductility of aluminum A356 by 5 times, and increases fatigue life in conventional welds [11].

2.2.1 Weld Microstructure

There has been significant interest in the microstructure resulting from FSW. There are four different regions in the weld microstructure as shown in figure 2.2:

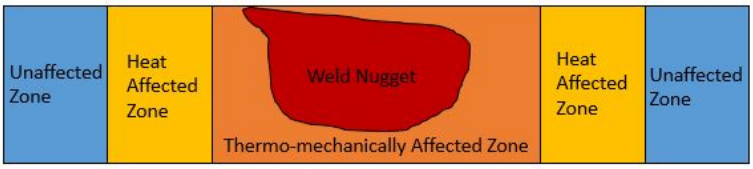

Figure 2.2: Diagram of microstructure resulting from FSP.

1. Weld Nugget: The center of the weld where the tool passes through is called the weld nugget. This region experiences the greatest strain, the highest temperatures and the most drastic transformation.

2. Thermo-mechanically Affected Zone (TMAZ): The region surrounding the weld nugget is called the thermo-mechanically affected zone. This region experiences some strain and elevated temperatures. There is a moderate amount of transformation in this region.

3. Heat Affected Zone (HAZ): The heat affected zone surrounds the thermo-mechanically affected zone and experiences elevated temperatures, but no strain. There is a small amount of transformation.

4. Unaffected Zone: The unaffected zone surrounds the heat affected zone and does not experience significant transformation.

2.2.2 Tooling

From its inception, FSW has been used mostly on softer metals such as aluminum and magnesium. Recently, tool advances have enabled FSW to be applied to harder materials, such as stainless steel [23,24]. There is a wide variety of materials that can be used to create tools for FSW. For softer materials such as aluminum and magnesium, high-strength steels are generally used for tooling material [13, 14, 25–27]. For harder materials such as stainless steels, polycrystalline cubic boron nitride (PCBN) is commonly used [19, 23, 28]. PCBN is an extremely hard material and can withstand very high temperatures, however it can easily fail during the plunging stage due to brittleness.

FSW tools have a shoulder that is slightly concave or convex with a pin protruding out of the center of the tool. A wide variety of tools have been used in FSW. The most notable feature is whether or not the pin is threaded. Threaded pins are believed to generate more downward force and increased temperature [29].

2.2.3 Industry Applications

FSW is being adopted into many different industries. Some example industries include automotive, shipbuilding, rail, and nuclear. Kallee provides an in-depth view into how FSW and its variants are being used [30]. A few examples are listed in this section.

Mazda used a revised version of FSW called friction stir spot welding (FSSW) in which the plunging stage of FSW is used to join metals at a point as opposed to a weld-line. Mazda used FSSW in 2003 on the backdoor of the RX-8 [31]. Mazda obtained 90% operation energy savings and greater than 40% capital investment reductions as compared to traditional resistance spot welding [32, 33]. They later used the same process on the MX-5 in 2005 [31].

Many components of ships are made of aluminum due to its high strength-to-weight ratio. Some of these components are joined using FSW. One of the major advantages of using FSW over fusion welding is its superior properties and strength. Since ships can go through difficult weather, it is important that components are joined with stronger techniques. [30, 34]

Nuclear waste is radioactive and needs to be stored with care. Sweden uses FSW to seal the lids on copper barrels containing nuclear waste [35]. Similar to aluminum, copper is an optimal material on which to use FSW because it is soft which will reduce tool wear. This means that the same tool can be used for many different welds which saves on the cost of tooling.

2.3 Simulating Friction Stir Welding

There are many methods to simulating FSW; however, the major two methods are FEA and computational fluid dynamics (CFD). Other modeling methods include thermal modeling and finite difference modeling.

2.3.1 Finite Element Analysis

FEA is used largely in solid mechanics especially structural applications and can model both static and dynamic systems. An advantage of using FEA over other modeling techniques is that local temperatures, stresses, strains, and strain rates over time can be estimated from which properties such as grain size and yield strength can be predicted locally.

In most FEA models, a Lagrangian-type simulation is used to model phenomena, in which the material and FEA mesh are coupled at the nodes [36]. In simulating processes with high deformation, such as FSW, the Lagrangian implementation will often produce ill-defined element shapes due to the coupling of meshes. These elements can then cause significant error in the final result. To remedy this problem, many FEA packages have introduced a remeshing operation that will generate a new mesh once the previous mesh becomes ill-defined. While this is an acceptable method to fixing the issues associated with large deformation simulations, it introduces operations that are very costly with respect to time.

Arbitrary Lagrangian-Eulerian (ALE) simulation methods have been introduced recently to create a marriage between Lagrangian methods and Eulerian methods in an attempt to maximize

the benefits of each while minimizing negative aspects [36–39]. In ALE methods, the material and mesh nodes at fixed boundary conditions are coupled while the free nodes are decoupled. This allows the mesh nodes to evolve in a way as to reduce ill-defined mesh evolution, saving copious amounts of time remeshing. The current thesis uses an Eulerian formulation that models the steady-state simulation [40].

There are many researchers who have created FEA simulations to investigate FSW. Many of the models were created to investigate temperature, strain rate, and material flow.

Very few researchers have investigated final grain size and yield strength after FSW using FEA. The large majority of these researchers used aluminum alloys as their subject material. Buffa et al predicted grain size in AA7075-T6 using 2 different analytical methods [41]. Fratini et al predicted grain size in AA2139-T8 using an artificial neural network with strain, strain rate, temperature, and the Zener-Hollomon parameter as inputs [42]. The artificial neural network was found to predict grain size with very good accuracy. Saluja et al created a cellular automata coupled finite element model to predict grain size and yield strength in Al6061-T6 [43]. Since stainless steel has significantly different characteristics than aluminum alloys there is a need to design predictive grain size and strength models for stainless steel.

2.3.2 Computational Fluid Dynamics

Many authors have used CFD as a modeling tool for FSW [44–48]. Similar to FEA, CFD models material movement, but uses different governing equations to predict what happens with the material. It is often used in pure fluid applications. CFD is often used to model FSW because the stir zone in FSW is in a plastic state that acts similar to both a solid and a liquid. Because of this behavior, the governing equations behind both FEA and CFD have difficulty modeling exactly what occurs in the FSW weld nugget. Often, the better modeling method depends upon what the researcher hopes to achieve from the simulation. The disadvantage of using CFD to model FSW is that CFD does not include critical material properties in its simulation calculations such as elasticity and being able to change the downward force. In this thesis, it was determined that FEA would provide more useful information than CFD.

2.3.3 Other Modeling Techniques

There are several alternative methods to simulating FSW. Thermal models have been used to simulate the temperature change caused by FSW [49, 50]. The advantage of a thermal model is that it is very simple to create and run. The disadvantage of thermal models is that it does not capture most of the complex phenomena that happens. For instance, strain is not found in these thermal model, but is one of the critical components of FSW.

2.4 Grain Growth

Grain growth occurs when metals are exposed to a combination of heat and work. There are two basic types of grain growth: static and dynamic. Static grain growth occurs when only heat is applied to the system and strain is not present. The general equation used for static grain growth is:

$$d = d_0 + K_0 t \tag{2.1}$$

In equation 2.1, d is the final grain size, d_0 is the initial grain size, K_0 is a material specific constant, and t is time.

Dynamic grain growth occurs when heat and strain are applied to the system. In FSW, dynamic grain growth occurs in the weld nugget and results in fine equiaxed grain shapes. The resulting grain size after dynamic recrystallization is in equation 2.2.

$$d = c_1 \dot{\varepsilon}^{c_2} \exp\left\{c_3\left(\frac{Q}{RT}\right)\right\} \tag{2.2}$$

In equation 2.2, d is the final grain size, $\dot{\varepsilon}$ is the strain rate, Q is the activation energy, R is the universal gas constant, T is the temperature, and c_1, c_2, and c_3 are material specific constants. For 304L SS, Venugopal and Sivaprasad found material constants and the activation energy for equation 2.2 for a strain rate range of $0.1 - 20s^{-1}$ and a temperature range of 950°C−1250°C [51]. Restrictive ranges in equations is a major drawback to using empirically derived equations.

In the material constants for 304L SS, c_2 and c_3 are negative. Therefore, higher strain rates will result in smaller final grain size and higher temperatures will result in larger final grain size.

One of the drawbacks of using empirical modeling techniques is that the constants are accurate only for a specific range of input material properties.

In FSW, the material initially experiences dynamic grain growth from the strain created by the rotating tool. The dynamic grain growth creates smaller grains in the microstructure. After the tool passes through the material, it will experience static grain growth which is mainly controlled by temperature and cooling rate.

2.5 Machine Learning in FSW

Very few authors have used machine learning to predict properties after or during FSW. A majority of these models are use a variant of feedforward artificial neural networks (ANNs) and are often coupled with other data acquisition methods. Rarely are other machine learning algorithms discussed in research even though many other powerful machine learning techniques exist.

Tansel et al created a series of ANNs that predict different properties after FSW. These ANN models fed into a genetic algorithm optimization with the objective of finding the optimal FSW parameters. The genetic algorithm then fed the ANNs a new set of FSW parameters. This was repeated until there was low output error [52].

A method to detect wormholes during FSW using a Fourier transform paired with a neural network is proposed by Boldsaikhan et al. The neural network takes in feedback forces from the FSW tooling and outputs the quality of the weld. Since the result is a binary value, the activation functions used are sigmoidal in nature [53].

Okuyucu et al used an ANN to predict mechanical properties after welding. The input variables included welding RPM and translational velocity and the outputs included tensile strength, yield strength, elongation %, and hardness. There were 20 different parameter sets used in this study [54].

Fratini et al created an ANN to predict the grain size distribution across the weld zone. In this study, a Lagrangian FEA simulation was developed to calculate processing data such as strain, strain rate, and temperature to use as the model inputs. The results of the ANN were compared with an empirically derived equation and was found to have greater accuracy [42]. The study did not used FSW specific parameters such as RPM even though several different parameter sets were used to train the models.

2.5.1 Random Forest Algorithm

Though useful, neural networks have two major disadvantages, The first is that they need significant amounts of data to make them worth using. The second is that it is easy to train the model to overfit the training data. The random forest algorithm used in this thesis can be used with much smaller data sets and is inherently resistant to overfitting in large part because it is an ensemble method using the bagging principle. In many cases, random forests can be just as accurate as neural networks with significantly less time spent in optimizing the model parameters. Virtually no research has been done on applying the random forest algorithm to FSW.

The random forest algorithm is an ensemble machine learning method which uses multiple decision trees to make an estimation. The random forest algorithm can be used for classification and regression. This thesis uses random forest for regression. An example of a simple decision tree is shown in figure 2.3 from EliteDataScience.com [55]. Each box is a called a node. At each node a split occurs which categorizes the data into two different buckets according to the splitting criterion. In a single decision tree the splitting criterion is developed though calculating the resulting entropy and creating the tree that minimizes entropy. In a random forest, the criterion are generated randomly.

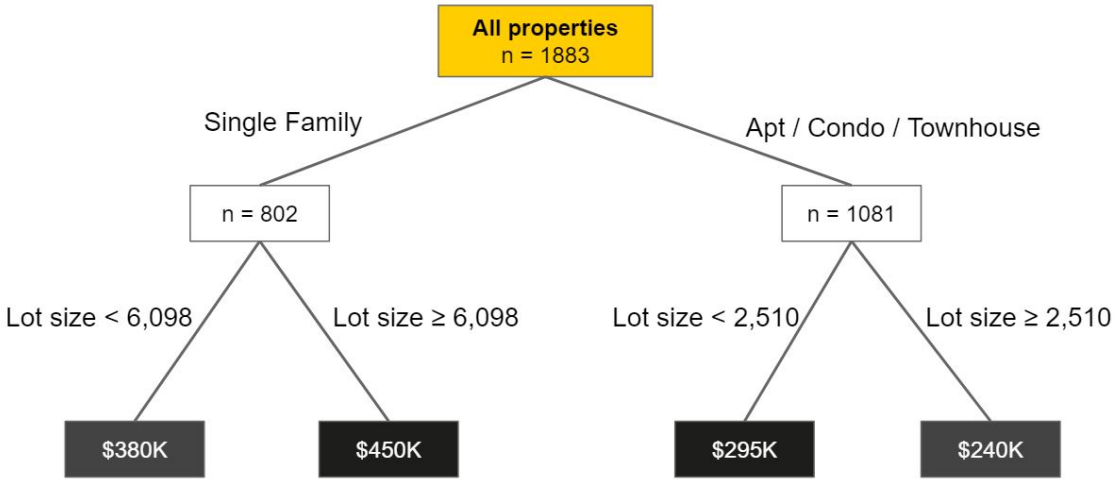

Figure 2.3: Example of a decision tree used for regression.

The decision tree functionally breaks a data set into regions with the value of each region being the average of the data in the region. An example of breaking the data apart is in figure 2.4.

In the random forest algorithm, the regional values of all the trees are averaged together to get the final value for a set of independent variables.

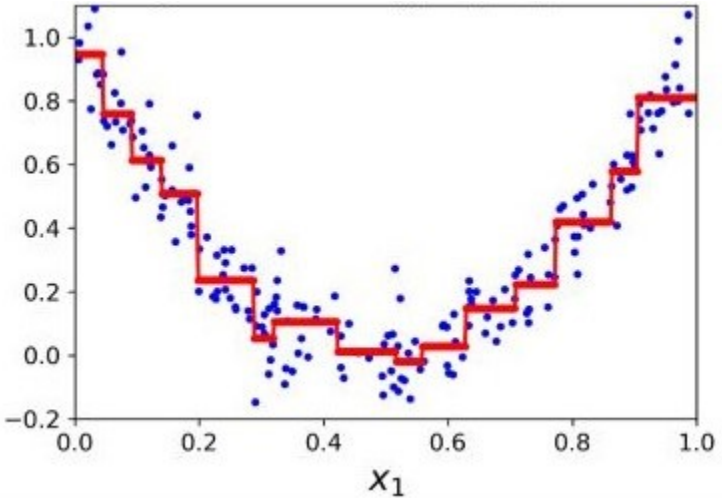

Figure 2.4: Example of how the decision tree breaks a data set into regions.

CHAPTER 3. METHODOLOGY

3.1 Friction Stir Processing Experiments

FSP experiments were done to gather data to validate the FEA models (FEMs). Many of the characteristics of FSP are hard to quantify and track experimentally, especially strain rate. One phenomenon that is easy to characterize is temperature; therefore, the temperature profile over time was used as the main validation technique for the FEA simulation. The strain rate was validated through comparing the values in the FEM to strain rate values in literature. This method of validating the strain rate will not ensure that the strain rates are completely accurate. Doing so would be beyond the scope of this thesis. Instead it will ensure that the strain rate is in the order of magnitude that other authors have predicted it to be.

3.1.1 Parameters

Only two sets of parameters were tested due to the complexity of adding additional parameter sets. For the first set, the translational velocity was 50 mm/minute and the rotational velocity was 80 RPM. For the second set, the translational velocity was 100 mm/minute and the rotational velocity was 250 RPM. The parameter sets will be referred to in this thesis as XXX/YYY where XXX is the RPM and YYY is the translational velocity in mm/minute (mmpm) (e.g. 80/50 for 80 RPM, 50 MMPM).

3.1.2 Tool Geometry

The tool used for the experiments was designed and manufactured by MegaStir Technologies and was optimized for superior FSW. The tool is called Q70 and is a tungsten-rhenium (W-Re) and PCBN composite. Many FSW tools have issues with endurance while welding a stronger steel such as stainless steel. However, Q70 was created to handle a large quantity of FSW runs of

stronger materials. The W-Re is a binder that increases ductility and decreases the catastrophic failure that is common in PCBN tools. It has a threaded pin which causes a downward velocity component while stirring, creating greater mixing of the weld zone. Threaded pins are thought to improve welding properties.

3.1.3 Temperature Profiles

Experimental temperature profiles were obtained only for the 250/100 set. This set was used to tune the FEM and then that model was modified to create the 80/50 model. The temperature profiles were obtained by placing thermocouples in the base material during friction stirring to record the temperature over time. The thermocouples were placed at 7mm, 9mm, and 11mm from the weld centerline on the advancing side. The experimental temperature profiles were compared to the profiles obtained from the FEM to determine if the model accurately represents the processing properties during welding. The error was found by comparing the peak temperatures of the experimental and FEM temperature profiles through equation 3.1.

$$Error = \left| \frac{Tmax_{Predicted} - Tmax_{Experimental}}{Tmax_{Experimental}} \right| \tag{3.1}$$

3.2 Finite Element Analysis Simulations

Finite element analysis models were set up to replicate the physical experiments in order to measure temperature and strain rate throughout the welding cross section. The simulation used the same parameters that were used in the physical experiments and were developed in the FEA program developed by TRANSVALOR called FORGE®. This program was chosen because of its superior ability to handle contact elements.

A specialized code was supplied to BYU by the Centre de Mise en Forme des Materiaux (CEMEF) in France. The code is an ALE formulation that enables an Eulerian approach to modeling FSP, which is especially helpful for modeling FSP in steady-state. With this model formulation, steady-state is represented by the last step in the FEA simulation and all prior steps are meaningless for purposes of analysis. The FEA mesh was refined locally behind the path of the

tool to improve the accuracy of the results. The mesh used tetrahedron shaped elements based on an enhanced (P1+/P1) element.

For this analysis, the plunging portion of the weld is not modeled because modeling the plunge would need to be a Lagrangian operation and the focus of this thesis is on the steady-state portion of FSW. The heat between the tool and the plate is modeled however to improve accuracy of the model.

3.2.1 Governing Equations

The weak form of the momentum equation used in this simulations is in equation 3.2 and the weak form of the incompressibility of plastic deformation is in equation 3.3.

$$\forall \mathbf{v}^* \int_\Omega \mathbf{s} \cdot \dot{\varepsilon}^* dV - \int_\Omega p \nabla \cdot \mathbf{v}^* dV - \int_\Omega \mathbf{T} \cdot \mathbf{v}^* dS = 0 \tag{3.2}$$

$$\forall p^* \int_\Omega p^* (tr\dot{\varepsilon} - \alpha T) dV = 0 \tag{3.3}$$

In equations 3.2 and 3.3 $\mathbf{s}$ is the stress deviator, $\dot{\varepsilon}$ is the strain rate tensor, p is the hydrostatic pressure, $\mathbf{T}$ is the surface traction, α is the coefficient of thermal expansion, and T is the temperature.

Equation 3.4 defines the stress deviator solution.

$$\mathbf{s} = 2K(\sqrt{3}\dot{\bar{\varepsilon}})^{m-1}\dot{\varepsilon} \tag{3.4}$$

In equation 3.4, K is a material dependent parameter defined by equation 3.5 where K_0 and β are material constants.

$$K = K_0(\varepsilon_0 + \bar{\varepsilon})^n e^{\frac{\beta}{T}} \tag{3.5}$$

Friction was defined by a viscoplastic Norton friction law. The shear stress component is modeled by equation 3.6 and the tangential component is modeled by equation 3.7.

$$\tau = \sigma_n - (\sigma_n \cdot n)n \tag{3.6}$$

$$\tau = -\alpha_f K \left| v_g \right|^{q-1} v_g \tag{3.7}$$

In equation 3.7, α_f is the friction coefficient, q is the sensitivity to sliding velocity, and v_g is the tangential velocity difference.

Equation 3.8 describes the heat generation resulting from the plastic deformation from the deformable plate.

$$\dot{q}_v = f\bar{\sigma}\dot{\bar{\varepsilon}} \tag{3.8}$$

The equivalent stress ($\bar{\sigma}$) component is defined by equation 3.9.

$$\bar{\sigma} = \sqrt{\frac{3}{2}\mathbf{s} : \mathbf{s}} \tag{3.9}$$

Equation 3.10 describes the heat generation between the tool and the deformable plate.

$$\dot{q}_f = \tau \cdot \Delta \mathbf{v}_s \tag{3.10}$$

Effusivity is defined by equation 3.11.

$$Effusivity = \sqrt{\rho c k} \tag{3.11}$$

3.2.2 Material Properties Sensors

FORGE® has a feature that allows users to place simulation sensors that detect material and simulation properties at every step during the computation. These sensors were placed in the simulated weld plate in a lattice-type structure so as to get the material properties throughout the plate. The total number of sensors used in the plate was 16,690 with the greater concentration in the weld nugget. Less than 10% of these sensors resulted in erroneous values and were dropped from the analysis. Linear interpolation was used to fill in needed values. There was not a significant effect on the results from these missing values.

3.3 Hardness Prediction

3.3.1 Experimental Hardness Map

The experimental hardness map was obtained for both parameter sets by Gunter [6]. This was done by cutting a cross section of the weld nugget out of the experiments and then polishing it until smooth. The sample was then tested for hardness using a microhardness tester. The tester was automated to find the hardness in a grid pattern with a spacing of $400\mu m$. The grid structure resulted in 1120 hardness points for each parameter set. The resulting hardness maps were measured on the Vickers hardness (HV) scale.

3.3.2 Empirical Equation

The empirical equation that was derived by Venugopal and Sivaprasad [51] and is shown in equation 3.12 with its derived constants. In equation 2.2, the activation energy (Q) is $310,000\frac{J}{mol-K}$ and R is the universal gas constant equal to $8.314\frac{J}{mol}$. Mathematically, this equation can only be applied in areas where $\dot{\varepsilon} > 0$ because equation 2.2 is undefined when $\dot{\varepsilon} = 0$ and $\dot{\varepsilon} < 0$ is not physically possible. Therefore, areas with low strain will be excluded. Since these constants have been derived with specific strain rate and temperature ranges, care needs to be exercised in applying the equation to areas outside these ranges.

$$d = 20,560\dot{\varepsilon}^{-0.3}\exp\left\{-0.25\left(\frac{Q}{RT}\right)\right\} \tag{3.12}$$

For purposes of comparing to the hardness graphs, the grain size is converted to hardness through a linear relationship found by Gunter [6] shown in equation 3.13. This relationship represents a high correlation with $R^2 = 0.94$ and therefore can be used to convert grain size to hardness with high confidence.

$$Hardness = 173.34(GrainSize)^{-0.5} + 157.79 \tag{3.13}$$

3.3.3 Random Forest Algorithm

The random forest algorithm was implemented using the *RandomForestRegressor()* function from the *scikit-learn* Python library. The most important consideration in training machine learning algorithms is ensuring that overfitting does not occur. The random forest algorithm is highly resistant to overfitting; however, steps were taken to ensure overfitting does not occur through using a training/testing split. In a training/testing split, the training data set is used to train the model and the testing data set is used to evaluate the quality of the model. If the model performs well with the testing data, then overfitting is likely not occurring. In this training/testing split, 67% of the data was randomly selected to use to train the model and the rest of the data was set aside to test the model for overfitting. This is a typical split ratio used in industry.

The main parameters that were tuned in the random forest model were the number of decision trees generated and the number of features used in each decision tree. Increasing the number of decision trees increases the accuracy of the algorithm in general. Tuning the number of features used in each decision tree can result in minimized overfitting.

The error measure that was used in training the random forest algorithm was mean squared error (MSE). The MSE is a common error method used in training and measuring performance of regression models and the mathematical form can be viewed in equation 3.14.

$$MSE = \frac{1}{n}\sum_{i=1}^{n}(Y_i - \hat{Y}_i)^2 \tag{3.14}$$

In equation 3.14, n is the number of experimental data points used in the error calculation, Y is an array of experimental output values, and $\hat{Y}$ is the predicted value corresponding to each value of Y. The MSE is always non-negative and the lower it is, the better predictor the algorithm is. The objective of iteratively training the random forest model is to tune the parameters of the model to decrease the MSE.

The R^2 metric was also used in training the model as an intuitive method to understand the goodness of fit. The R^2 is a normalized MSE and can be viewed in equation 3.15. In equation 3.15, $\bar{Y}$ is the mean of all values.

$$R^2 = 1 - \frac{\sum_{i=1}^{n}(Y_i - \hat{Y}_i)^2}{\sum_{i=1}^{n}(Y_i - \bar{Y})^2} \tag{3.15}$$

The independent variables were selected through evaluating the cause that potential processing parameters would have on the final hardness. The three major mechanical causes of grain size are grain size after dynamic processing, temperature, and amount of time at temperature. The strain rate variable is highly correlated with the grain size after dynamic processing. The cooling rate determines the time that the material will be at elevated temperature.

CHAPTER 4. RESULTS AND DISCUSSION

4.1 FEA Model Formulation

The FEM was created with 5 different parts: the tool holder, the FSP tool, the deformable plate, the backing plate, and the backing plate holder. The FEA simulation is displayed in figure 4.1. The thermal properties of the parts that were used in the simulation are shown in table 4.1. Figure 4.2 contains a view of the mesh with the FSP tool traveling toward the picture.

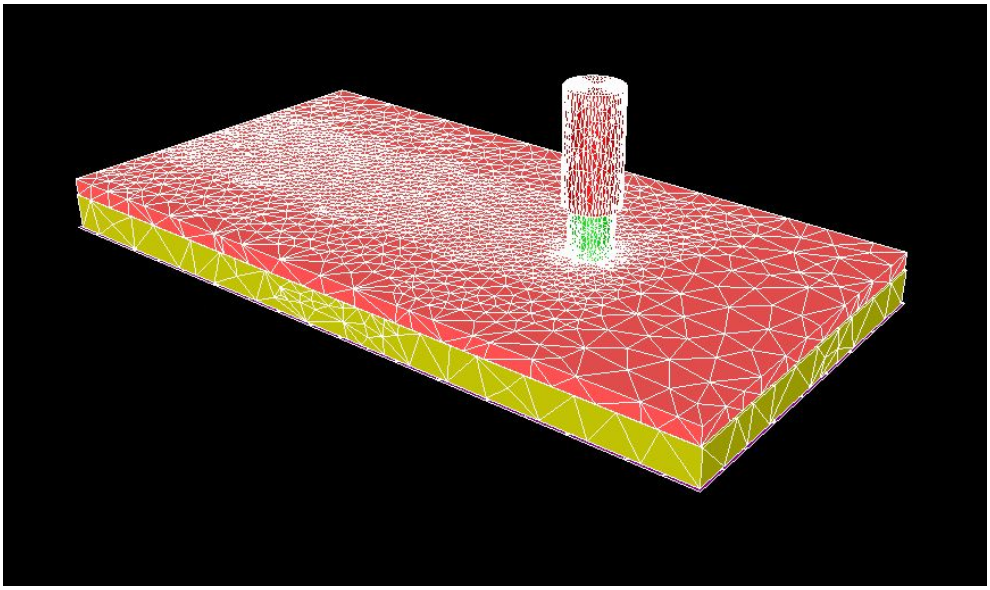

Figure 4.1: A picture of the FEA mesh. Parts from top to bottom: tool holder (red), FSP tool (green), deformable plate (red), backing plate (yellow), and backing plate holder (purple).

One issue with replicating the experiments with the FEM is the complex geometry of the tool pin. The experimental tool had a threaded pin to improve material flow. In FEMs it is difficult to simulate complex geometries such as threaded tools. To compensate for this, a velocity boundary condition was attached to the FEA tool pin to simulate the effects of the experimental threaded tool.

Table 4.1: Thermal properties for FEM parts.

	FSP Tool	Deformable Plate	Backing Plate
Conductivity $(10^4 \times W/mm^2K)$	13.0	2.80	5.90
Heat Capacity $(10^8 \times mm^2/s^2K)$	19.7	7.78	7.78
Density $(10^{-6} \times g/mm^3)$	3.12	7.85	7.85

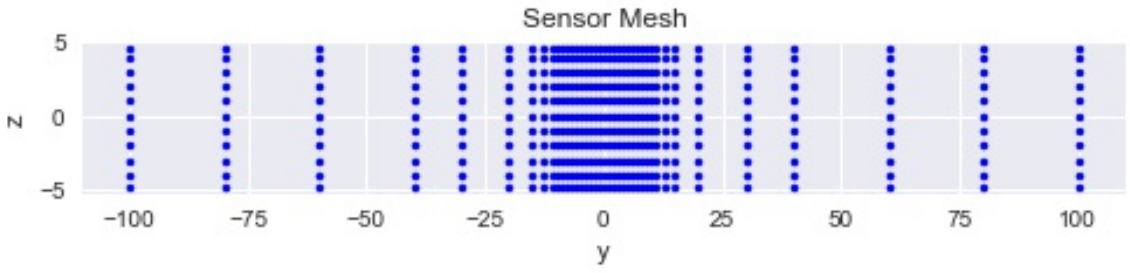

Figure 4.2: The FEM sensor mesh with the tool traveling in the direction of the picture.

4.2 FEA Model Validation

The temperature and strain rate from the FEM were validated for accuracy before use in the random forest model.

4.2.1 Temperature Validation

The FEM was validated by comparing the peak experimental and simulated temperature at three separate distances from the weld centerline: $7mm$, $9mm$, and $11mm$. To improve the temperature fit, the friction coefficient between the tool and the deformable plate was modified until the error was minimized. The friction coefficient between the tool and the plate is difficult to measure experimentally. The final coefficient was $\alpha = 0.1$.

The resulting temperature profiles are shown in figure 4.3. The lower time on the graphs represent the upstream material that has not been processed yet. The peak temperature represents the temperature felt at the point where the tool crosses the sensor. The higher time represents the heat dissipating after being processed. Visually, the experimental and simulated temperature profiles in figure 4.3 are very similar.

The errors resulting from equation 3.1 are listed in table 4.2 for each of the distances from the weld centerline. The errors at $y = 7mm$ and $y = 9mm$ represent a good fit. The largest error is at

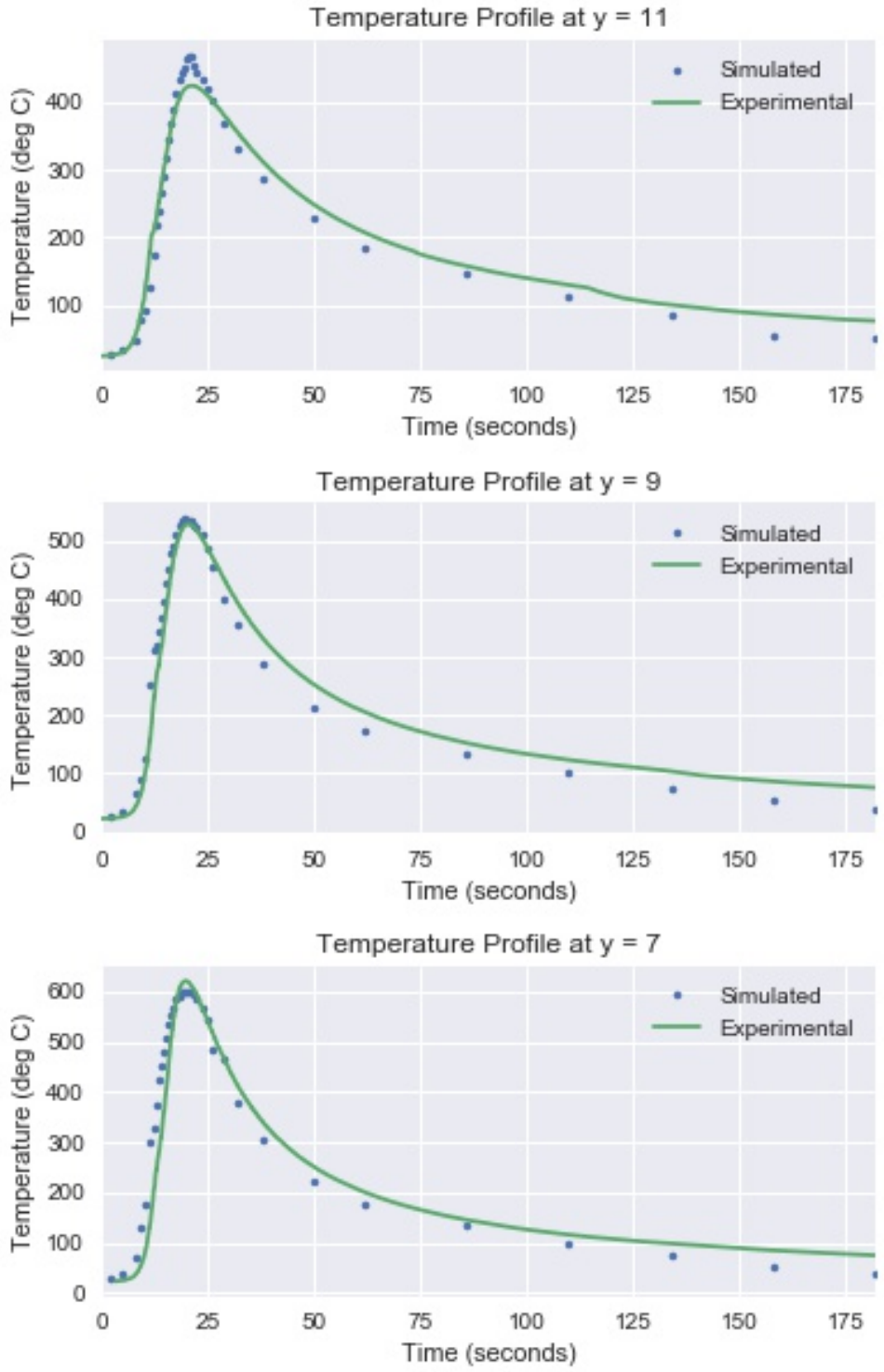

Figure 4.3: Temperature profiles at down 3 different lines parallel to the weld centerline. Low time represents material to be welded and high time represents material that has already been passed by the welding tool.

$y = 11mm$ where the peak simulated temperature is higher than the peak experimental temperature by 10.5%. The greatest interest of this thesis lies in the $y = -10mm$ to $y = 10mm$ range because that region represents the weld nugget. Due to this, the temperature data from the FEMs was used despite the moderate temperature error at $y = 11mm$.

Table 4.2: This table displays the error of the peak of each predicted temperature profile as com-pared to the experimental curve.

Distance from the weld centerline	7mm	9mm	11mm
Error (%)	3.1	1.8	10.5

4.2.2 Strain Rate Validation

The strain rate is very difficult to measure experimentally in FSW. However, many authors have calculated the strain rate through FEA simulations, CFD simulations, or calculation using the Zener-Hollomon parameter. Strain rate values that other authors have found are listed in table 4.3. The 80/50 model in was found to have strain rates of $0-2.48s^{-1}$ and the 250/100 model was found to have strain rates of $0-9.1s^{-1}$. Since the temperature from the FEM had acceptable accuracy and the strain rates for this thesis were in the range of strain rates that other authors have found, the strain rates calculated by the FEM were used.

Table 4.3: Reported strain rates for FSW in the scientific literature.

Author	Material	Strain Rate Value (s^{-1})
Coleman and Shercliff [44]	AA5083/AA7075	2
Sabooni et al [56]	304 stainless steel	2.57
Masaki et al [57]	AA1050	2-3
Jata and Semiatin [17]	Al-Li-Cu Alloy	10
Frigaard et al [58]	AA6082/AA7108	1-20
Current Thesis	**304L stainless steel**	**0-9.1**
Current Thesis	**304L stainless steel**	**0-2.48**

4.3 Temperature Results

The resulting temperature overlaid on the FEM is shown in figures 4.4 and 4.5. In each figure, the 80/50 set is displayed in subfigure (a) and is the top image. In figure 4.5, the temperature was shown to be lower in the pin than the shoulder by the temperature contours in both parameter sets. This is consistent with both literature and theory. Heat is generated in the weld nugget through plastic deformation as the grains are dynamically recrystallized. Higher velocity drives greater plastic deformation. Therefore, the tool shoulder, which has a higher absolute velocity because of the greater radius, generates higher temperatures than the pin which has a lower absolute velocity.

There were some slight temperature fluctuations in the tool keyhole. These fluctuations are probably due in part to the imperfect contact between the tool and deformable plate in the FEM. In a Lagrangian formulation, the tool would actually rotate at each step through time and any contact issues would resolve themselves. With the Eulerian formulation, the tool does not rotate through at each step so any contact issues between parts will permeate through the calculations.

There were significant differences in the temperature profiles between the different parameter sets in figure 4.5. The 250/100 set had a much longer temperature profile than the 80/50 set due to the faster translational tool velocity in the former set. The higher RPM in the 250/100 set also generated higher overall temperatures in the weld nugget

The temperature cross section of the tool is shown in figure 4.6. The red portion of the top of both figures is the tool. In figure 4.6(a) the max temperature was 808°C for the 80/50 set and in figure 4.6(b) the max temperature was 888°C for the parameters 250/100 set.

In figure 4.6(b), there was evidence of downward material flow at the bottom of the tool pin from the higher temperature material at the bottom of the pin. The material flow was due to the downward velocity component attached to the FEA tool pin which is simulating the threaded tool used in the experimental runs. The high material flow is juxtaposed to figure 4.6(a) in which there seems to be very little downward material flow.

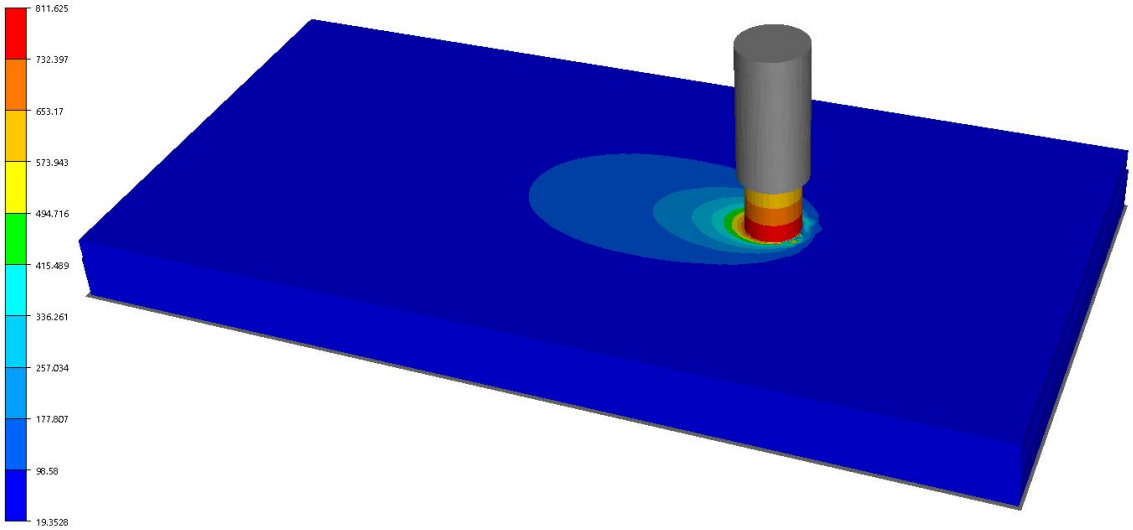

(a) Image of the final temperature with the tool for the 80/50 parameter set.

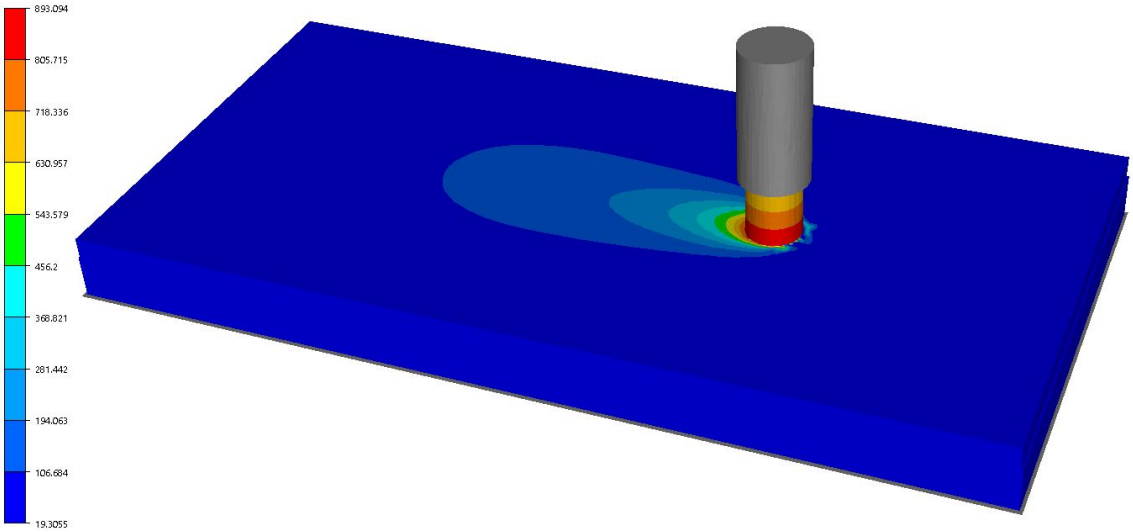

(b) Image of the final temperature with the tool for the 250/100 parameter set.

Figure 4.4: The FEM with the temperature overlaid on the model including the tool.

4.4 Strain Rate Results

Top views of the strain rate overlaid on the FEM are displayed in figure 4.7. The location of the maximum strain rate was at the front of the pin under the shoulder. This is because the pin is putting pressure on the front of the pin because of the forward translational velocity. The material is then pushed around the pin from the viscoplastic friction that occurs between the tool and the plate. The 250/100 FEM had significantly greater strain rate than the 80/50 FEM due to the higher translational velocity.

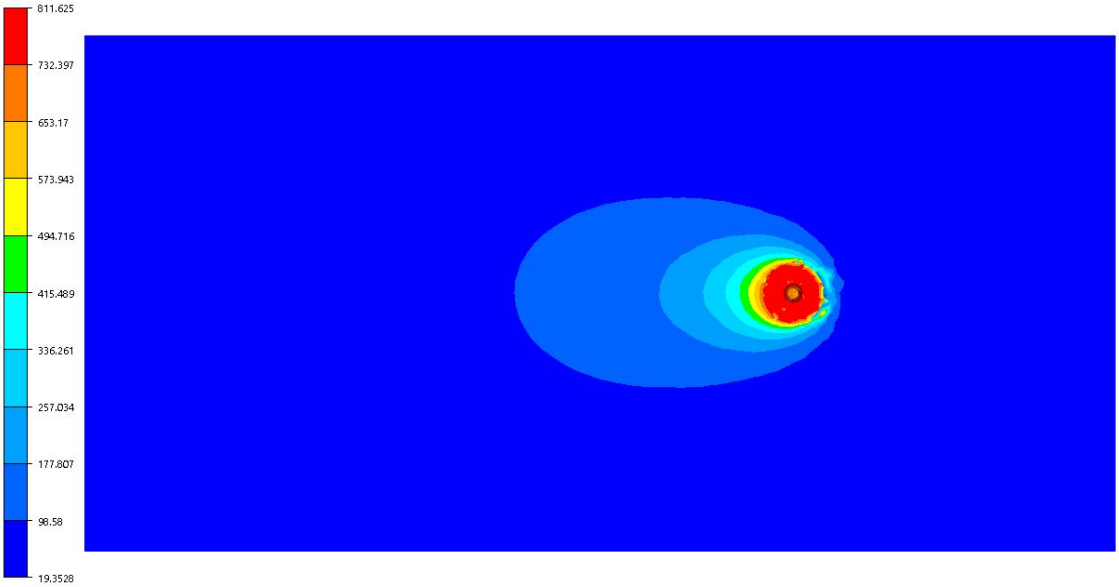

(a) Top view of the temperature overlaid on the 80/50 FEM.

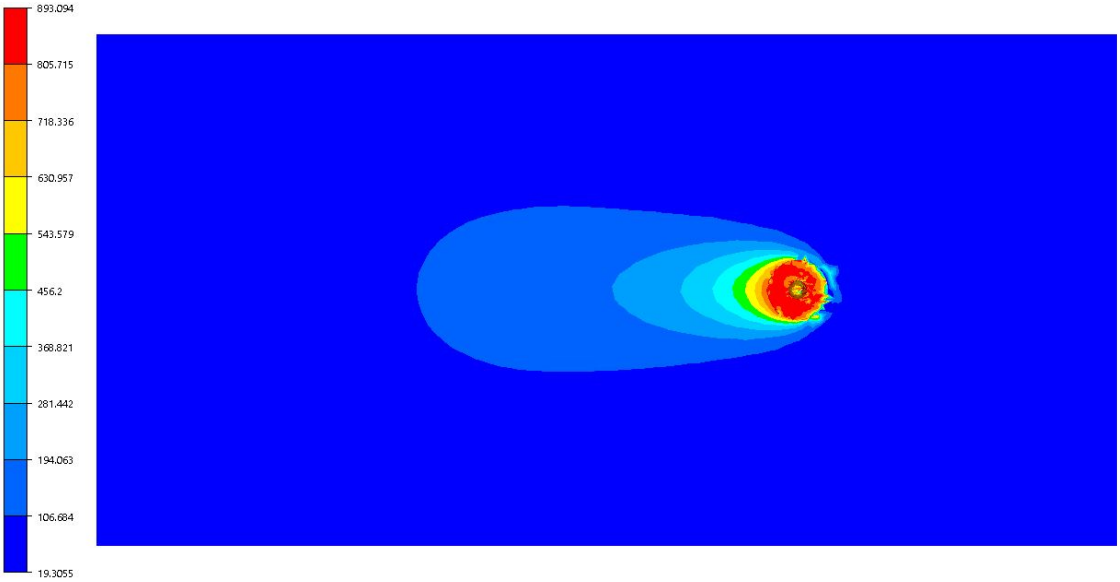

(b) Top view of the temperature overlaid on the 250/100 FEM.

Figure 4.5: A top view of the temperature overlaid on the FEM.

4.5 Hardness Maps

Hardness is related to the grain size through the Hall-Petch Relationship in equation 4.1. The smaller the grain size, the higher the tensile strength and hardness.

$$\sigma_y = \sigma_o + \frac{k}{\sqrt{d}} \tag{4.1}$$

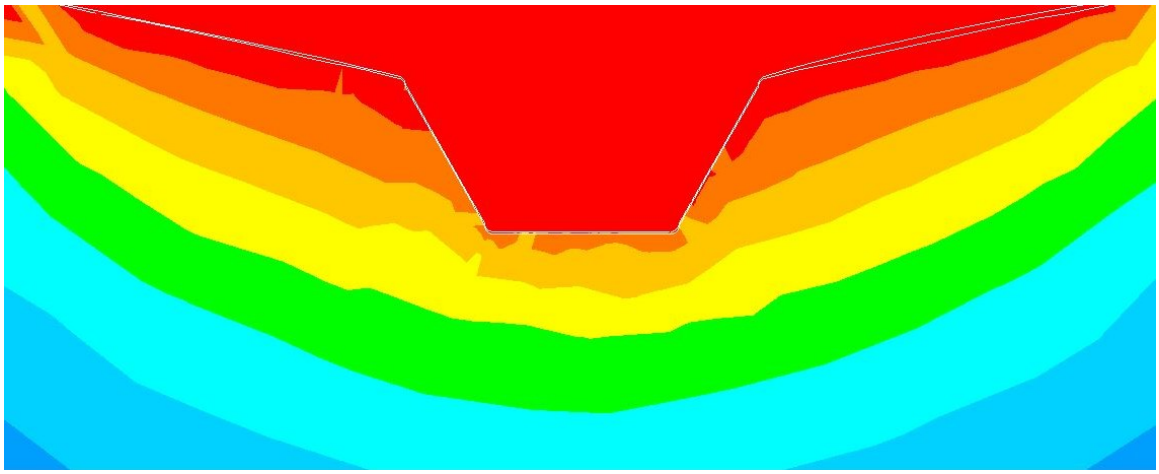

(a) Cross section of the weld displaying the temperature for the parameter set 80 RPM, 50 MMPM.

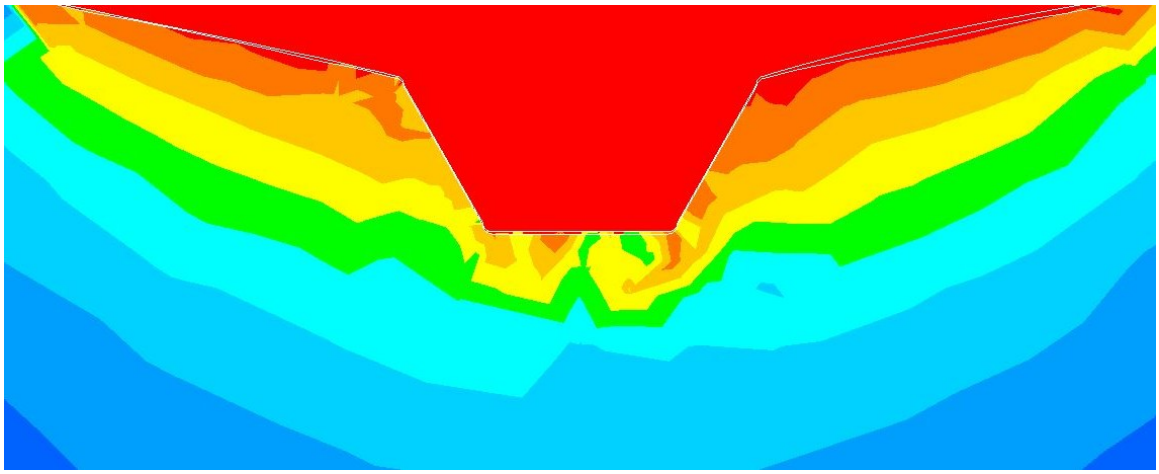

(b) Cross section of the weld displaying the temperature for the parameter set 250 RPM, 100 MMPM.

Figure 4.6: A view of the temperature of the cross section of the weld. The temperature contours are not on the same scale. Subfigure (a) has a lower temperature than subfigure (b).

The experimental hardness between the two parameter sets differs significantly. The hardness maps can be viewed in figure 4.8 for both parameter sets. The hardness maps are on the same hardness scale. The 80/50 hardness map was much harder than the 250/100 hardness map. This hardness difference was partially due to the difference in annealing effects that each parameter set will experience. The 80/50 set was welded at a much lower temperature; therefore, the grains had very little time to anneal at elevated temperatures relative to the 250/100 set. The 250/100 set experienced higher temperatures and thus had greater time to anneal at elevated temperatures, resulting in softer material.

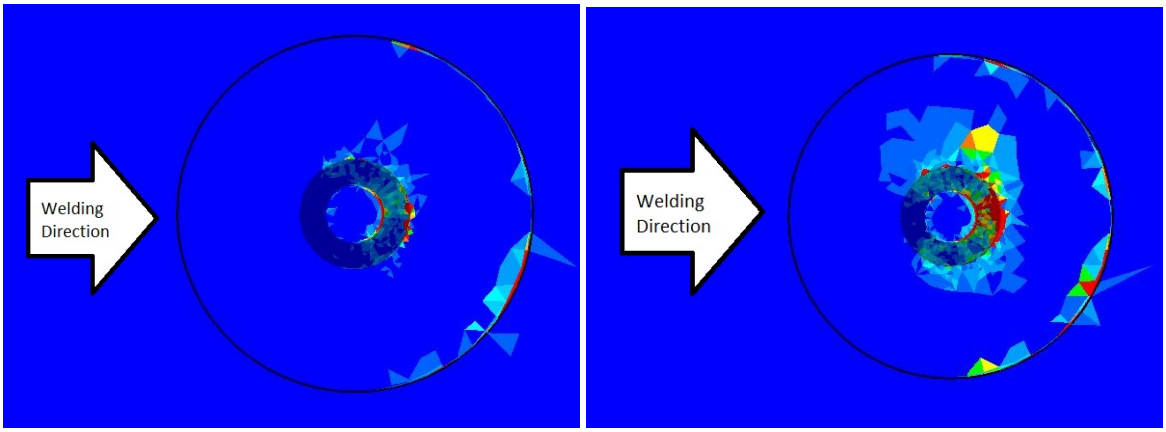

(a) Top view of strain rate from the 80/50 FEM. (b) Top view of strain rate from the 250/100 FEM.

Figure 4.7: The strain rate shown on the FEM. The red areas represent strain rate of $2s^{-1}$ or above in both figures.

As expected, there is a noticeable difference in the hardness between the processed area and the unprocessed area in the 80/50 parameter set. However, in the 250/100 set, the hardness difference was much less apparent. Much of the 250/100 hardness map had similar hardness to the HAZ and base material.

4.6 Random Forest Model

The inputs for the random forest model were determined to be temperature, strain rate, cooling rate ($\dot{T}$), and RPM. The temperature and strain rate were selected by filtering f or the maximum for each along the welding direction. In other words, the peak temperature and the peak strain were used at each point along the cross section of the weld. The cooling rate was approximated as a linear function and was calculated by equation 4.2.

$$\dot{T} = \frac{T_{max} - 100}{X_{T_{max}} - X_{T_{100}}} \tag{4.2}$$

In equation 4.2, T_{max} is the max temperature, 100 is the temperature in degrees Celsius where grain growth becomes insignificant, $X_{T_{max}}$ is the distance where the max temperature is, and $X_{T_{100}}$ is the distance behind the tool pin where the temperature is 100°C.

The cooling rate was chosen as a variable because the material inside the weld would experience greater insulation and, in effect, a lower cooling rate than material on the outside of

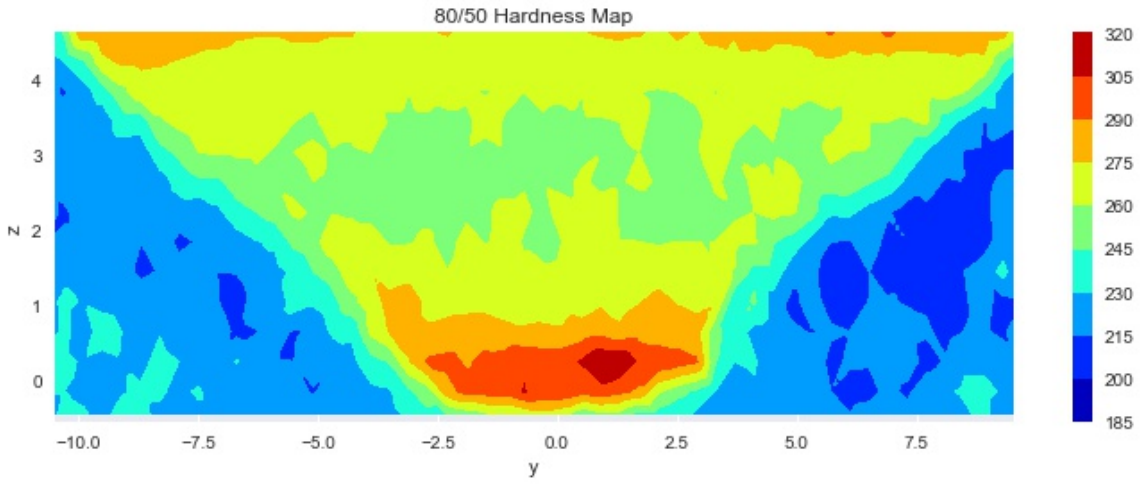

(a) Experimental hardness for the 80/50 set.

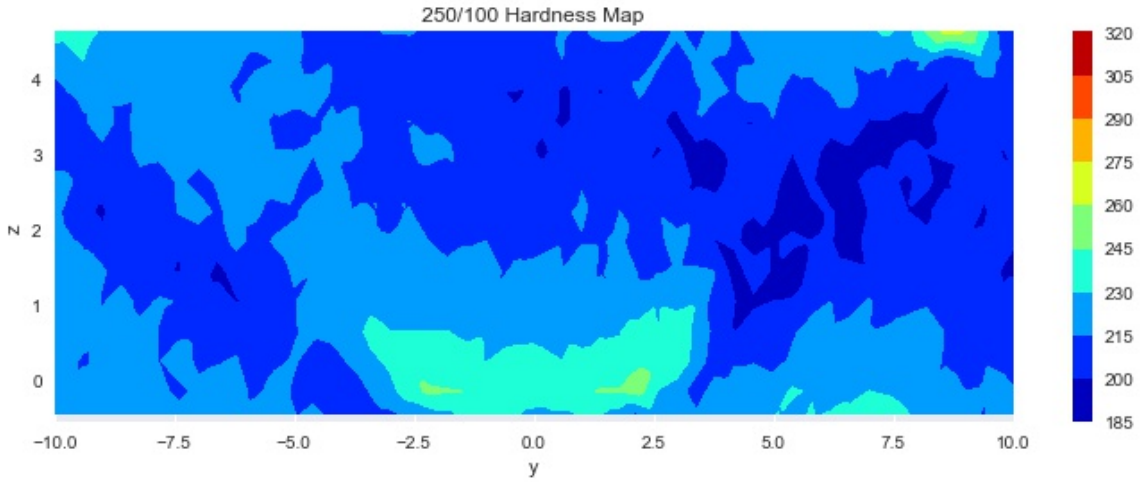

(b) Experimental hardness for the 250/100 set.

Figure 4.8: A view of the cross section for the experimental hardness. Both images are on the same scale.

the weld. The lower cooling rate would increase time at elevated temperature resulting in lower hardness. The max temperature would not compensate for the cooling rate since it is only one value at one time and it does not contain information about how fast the material would cool.

The RPM was selected as the only FSP specific parameter. Since this data set contains two welding parameters, the RPM acts similarly to a binary variable. If more welding parameters were added to the data set, RPM would become more of a continuous variable. The translational velocity was not used since it would be the same variable as the RPM in this case.

4.6.1 Variable Relationships

To determine any correlations between hardness and input variables, the data was graphed and is shown in figure 4.9, 4.10, and 4.11 for the 80/50 set, the 250/100 set, and the full data set respectively. The RPM was not included in the scatterplot matrices because it acts like a binary variable and would not be useful to see its relationships to the other variables. The strain rate was transformed to be on a natural log scale to improve the fit.

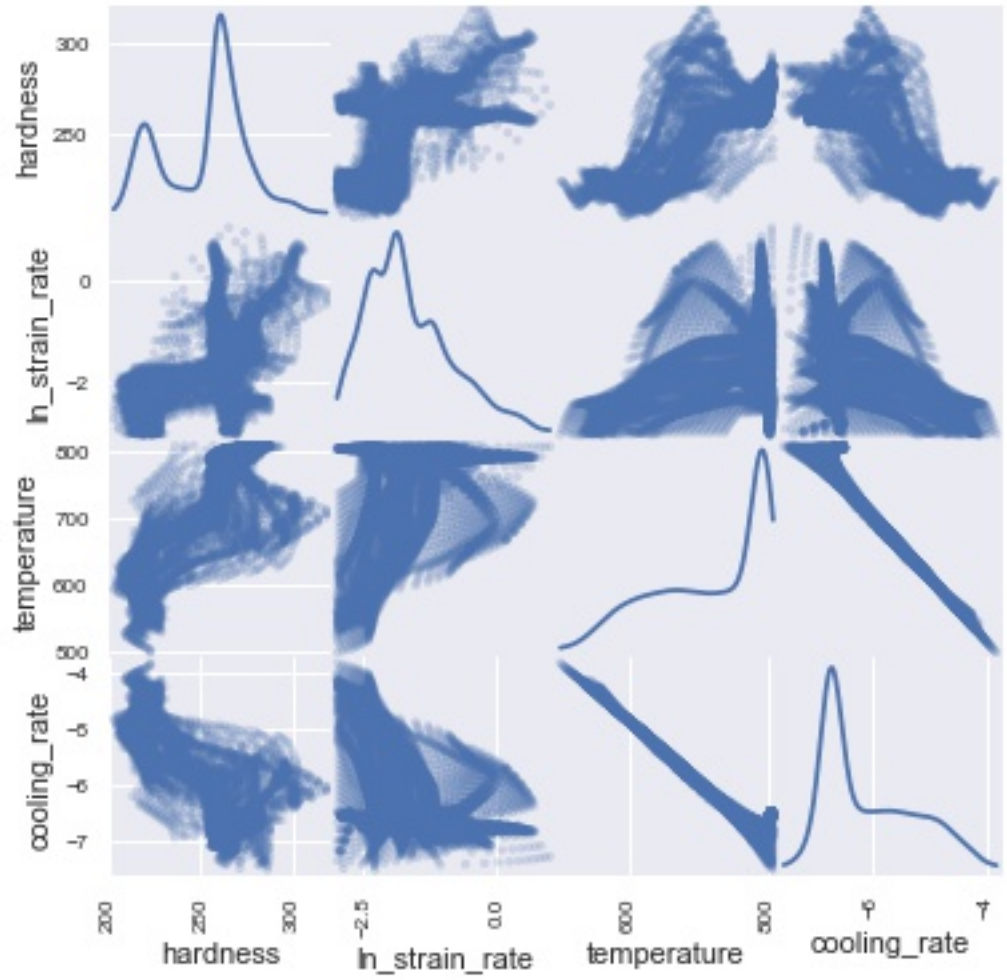

Figure 4.9: A correlation matrix displaying the relationships between variables for the 80/50 data set.

In the 80/50 model from figure 4.9, the relationships between hardness and the other variables had a slightly sigmoidal shape. However, even using a sigmoidal shaped function, it would be difficult to obtain a good approximation of the relationships. The strongest relationship was between the max temperature and cooling rate variables. It is expected that there is a relationship between these variables since they both are related to temperature of the weld and the max temperature would have some effect on the cooling process.

Since the temperature and cooling rate were highly correlated, our model contains multicollinearity. Multicollinearity occurs when one independent variable can be estimated using one or more independent variables. Multicollinearity disrupts metrics that evaluate the performance of independent variables in predicting the dependent variable such as p-values. However, as is well known that multicollinearity has no effect on the ability of a the independent variables to predict the dependent variable in most statistical tools including the random forest algorithm. Therefore, the models were trained with both the temperature and cooling rate in the final predictive model. However, the models were also trained without the cooling rate to see the impact of temperature, strain rate, and RPM in predicting hardness with the random forest algorithm using the feature importance metric (see figure 4.13).

In the 250/100 model from figure 4.10, the relationships between cooling rate and max temperature and the temperature and natural log strain rate were similar to those in the 80/50 model. However, the relationships between hardness and the independent variables were not easily discernable and did not have a distinct shape. While machine learning can be used to find complex relationships between variables, it is more difficult if there is no strong relationship between the independent and dependent variables.

In the full model in figure 4.11, the data from both sets were mixed. The hardness relationship with the independent variables was very complex and not easily modeled in one dimension. The scatterplot matrices in figures 4.9, 4.10, and 4.11 highlight the potential usefulness of machine learning in predicting final properties of FSP. It is difficult for humans to detect complex patterns especially in multiple dimensional data; however, machine learning is used in the very application of detecting complex relationships between variables, especially in multiple dimensions.

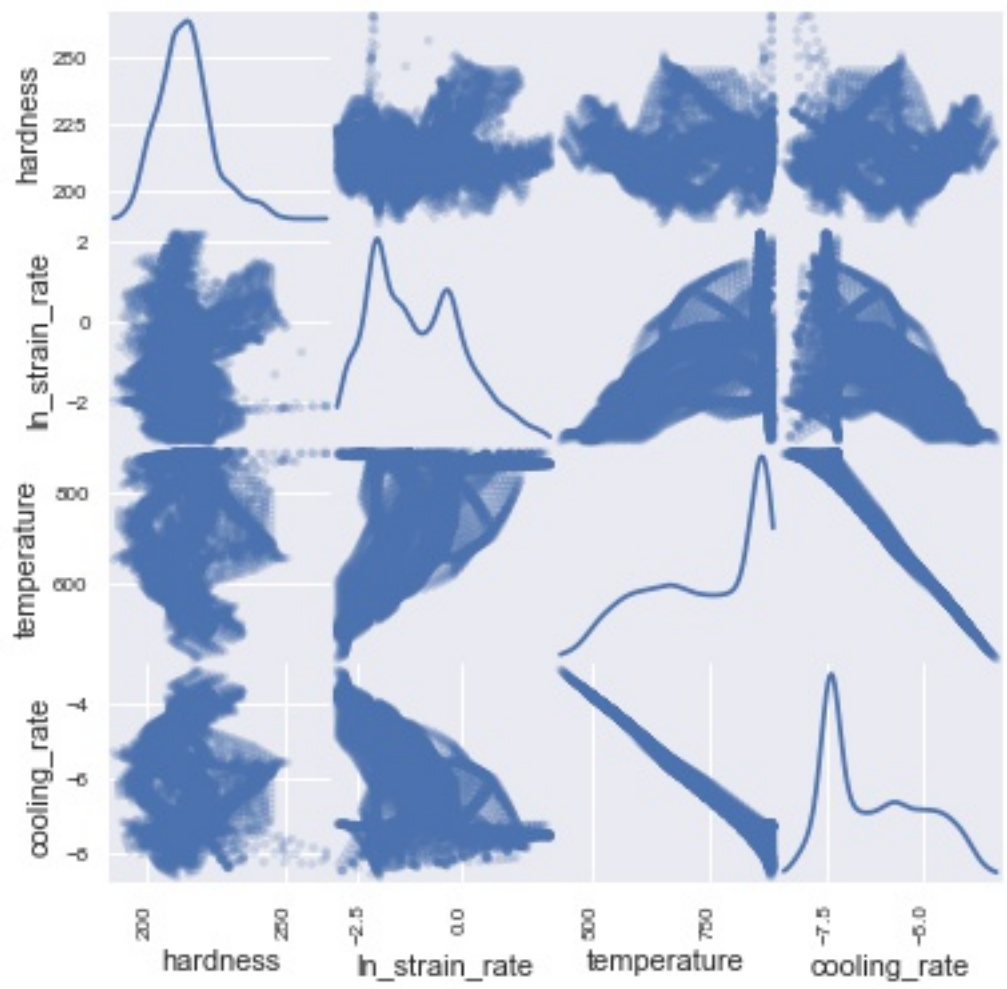

Figure 4.10: A correlation matrix displaying the relationships between variables with both the 250/100 data set.

4.6.2 Training the Model

Three different models were trained in order to evaluate the performance of the random forest algorithm:

1. Full model: Includes data from both parameter sets and is closest to a generalized model.

2. 80/50 model: Includes data from the 80/50 set.

3. 250/100 model: Includes data from the 250/100 set.

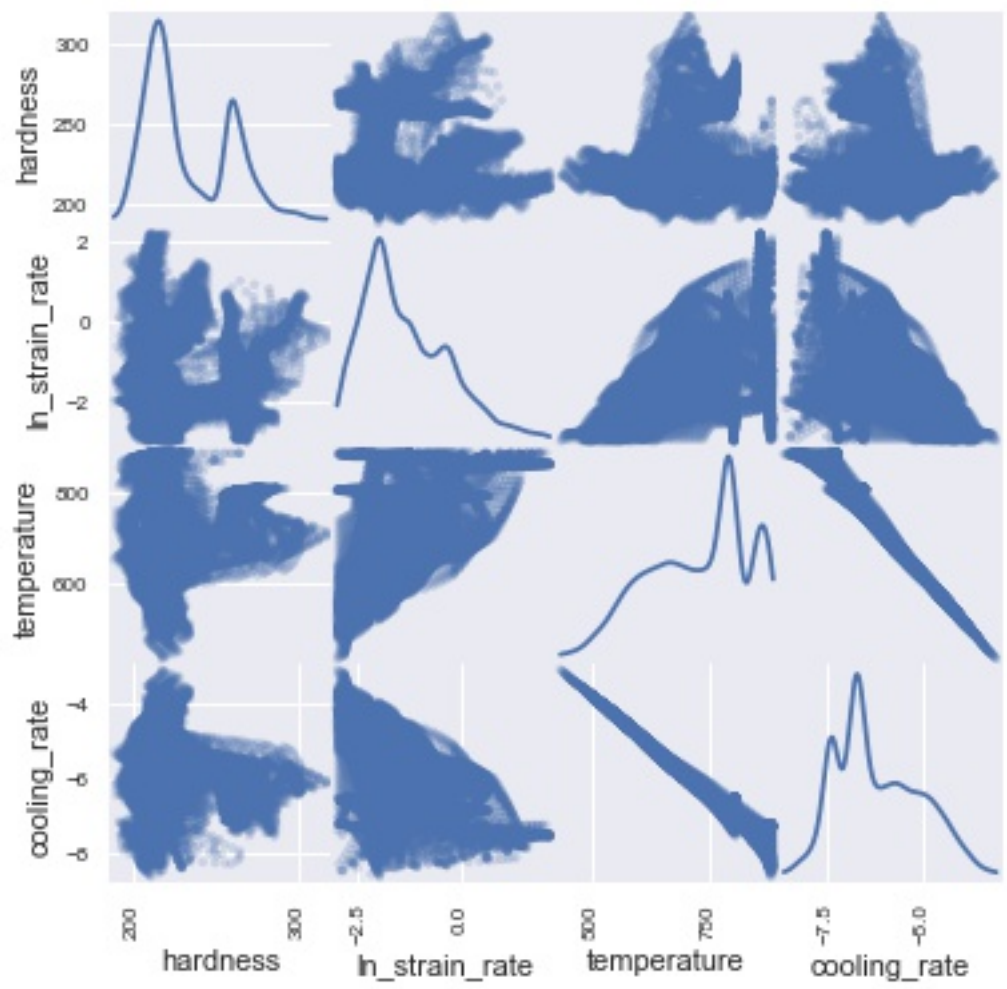

Figure 4.11: A correlation matrix displaying the relationships between variables with both the 80/50 and 250/100 data.

While the full model is the most important model because of its ability to predict multiple parameter sets, the single parameter models will be used to discover if different variables matter more for certain parameter sets. RPM was only used in the full model since the value would be the same for each observation for the single parameter models and would have no effect.

The *RandomForestRegressor()* Python function has many different parameters that can be tuned to improve model fit. Most of these parameters are used to tune models with many inputs. In this case, the main parameter that was changed to improve model accuracy was the number of estimators (i.e. decision trees) used in the model. The number of estimators that were tested ranged from 1 to 1000. Figure 4.12 displays the mean squared error and the R^2 value for the full model varying the number of estimators.

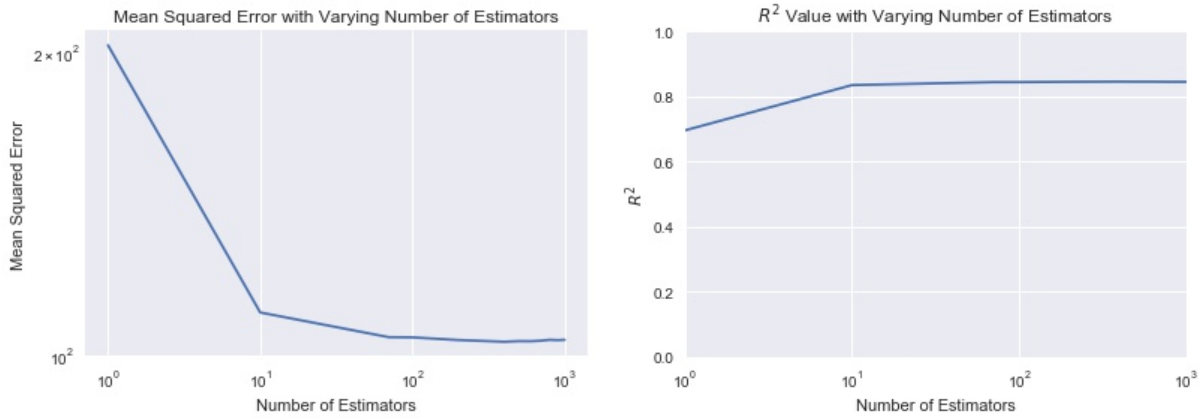

(a) The mean squared error of the training process.

(b) The R^2 value of the training process.

Figure 4.12: The mean squared error and the R^2 value decreases as the number of estimators increases with diminishing returns after 100 estimators.

The number of estimators had a significant impact on both the mean squared error until 100 estimators. Diminishing returns occurred after 100 estimators. Unsurprisingly, the R^2 value exhibited similar behavior to the mean squared error. In addition, there was a large increase in compute time when the number of estimators was above 500. Therefore, the models were trained with 100 estimators to save on computation time without having a significant effect on accuracy.

The R^2 values for each of the three models are listed in table 4.4. An important note to make is that the full model had twice as much data as the other two models because it was comprised of both parameter sets. The full model and the 80/50 model had very high R^2 values while the 250/100 model had a relatively low R^2 value. The full model performed the best, which is partially due to the greater number of data points it was trained with.

Table 4.4: The performance of each model measured by R^2.

Model	Full	80/50	250/100
R^2	0.95	0.93	0.64

Table 4.5 displays the R^2 value of the prediction of each model on individual parameter sets. Both the full and 80/50 models predicted the 80/50 data set very well. The full model had much lower accuracy in predicting the 250/100 set, but is still considered to have high accuracy.

Table 4.5: The mean squared error of the models predicting individual parameter sets.

Parameter set	Full	80/50	250/100
80/50	0.96	0.93	–
250/100	0.83	–	0.64

It is mathematically improbable that the full data set would predict the 80/50 data set better than the 80/50 model. It is a point of confusion of this thesis that the full model had better predictive power in this case.

4.6.3 Feature Importance

The models were run without the cooling rate variable to see the impact each feature had without the effects of multicollinearity on the analysis using the feature importance metric. The R^2 values for the full and 80/50 data set did not change significantly when cooling rate was removed; however, the R^2 value for the 250/100 model changed to 0.55. The feature importance for each model is displayed in figures 4.13.

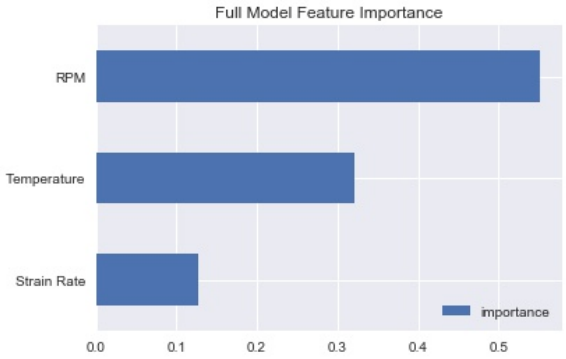

(a) Feature importance for the full model.

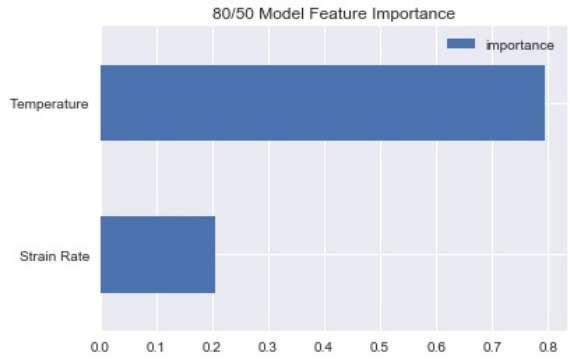

(b) Feature importance for the 80/50 model.

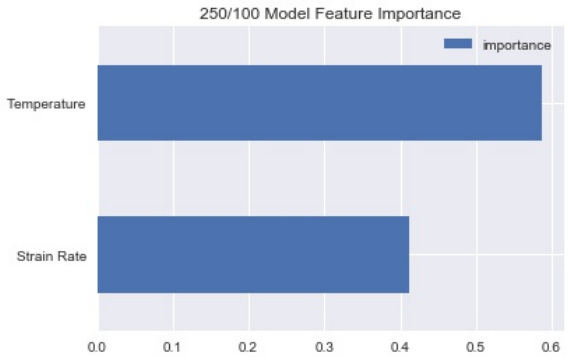

(c) Feature importance for the 250/100 model.

Figure 4.13: Feature importance for each model. The cooling rate has a significantly greater effect for data sets with greater hardness variance.

There were two interesting observations from the feature importance figures. The first was that RPM was of most importance in a multiple parameter model. If more parameter sets were included in the analysis, it could be possible that translational velocity could be of similar importance to RPM.

The second observation was that the temperature was the major factor in the single parameter models in predicting hardness. Strain rate varied significantly between the two data sets, giving evidence that there were slightly different mechanisms in the two parameter sets that determined final hardness.

4.6.4 Model Evaluation

The full model was used to predict the hardness maps for both parameter sets. The predicted and experimental hardness maps for the 80/50 set and the 250/100 set are in figures 4.14 and 4.15 respectively. All hardness maps use the same hardness scale. Overall, the model was effective at predicting the hardness maps in both structure and values.

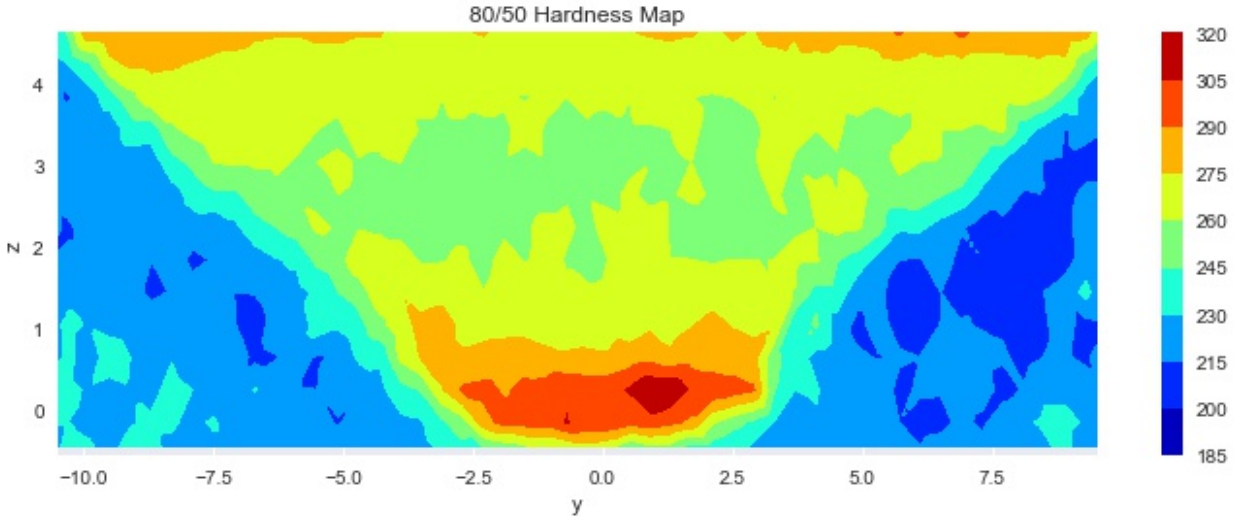

(a) 80/50 hardness map.

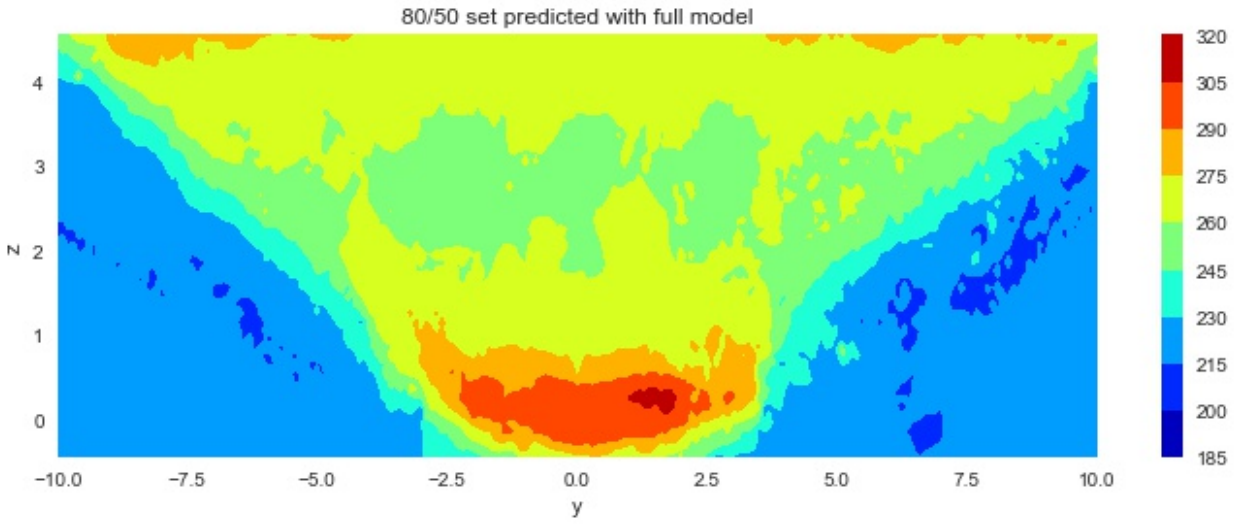

(b) Random forest predicting 80/50 hardness map.

Figure 4.14: Comparison of the 80/50 experimental and predicted hardness map.

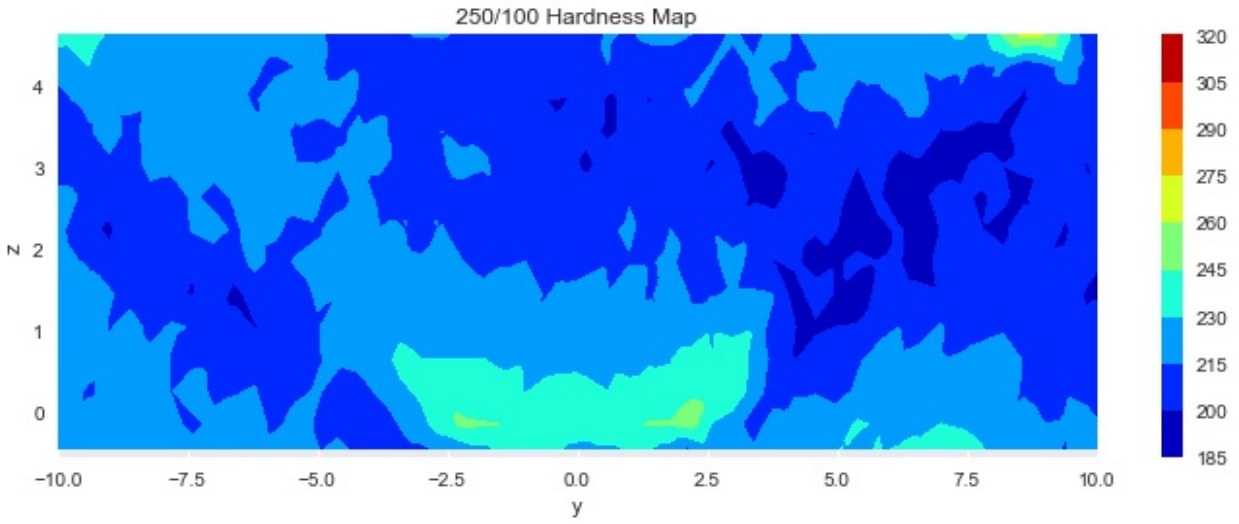

(a) 250/100 hardness map.

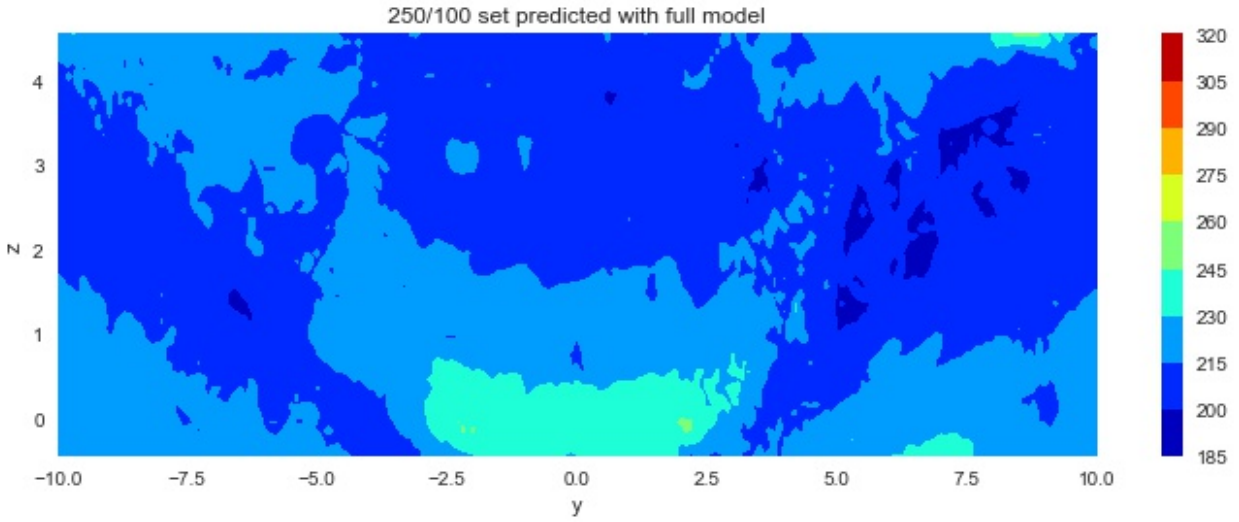

(b) Random forest predicting 250/100 hardness map.

Figure 4.15: Comparison of the 250/100 experimental and predicted hardness map.

There are some differences in the predicted graphs. The predicted maps generally had much smaller islands of points where the hardness will suddenly spike. A good example of this was on the advancing side of the weld in the 80/50 map where there were many small light blue islands in the predicted graph relative to the experimental graph. The random forest prediction seemed to predict the softer areas harder than they are and the harder regions as softer than they actually are. This trend was especially apparent in the HAZ and the bottom of the weld nugget. The HAZ in both figures was slightly harder in the predicted graph. The weld nugget was slightly softer in

the predicted graphs than the experimental. In essence, the random forest seemed to average or smooth the hardness over the graph.

The hardness map for the 250/100 parameter set derived from the empirical equation is displayed in figure 4.16. The hardness map was filtered to include only those strain rates greater than $0.1s^{-1}$. The temperature was not restricted because none of the material experienced temperatures above 900°C; therefore, the hardness map would not exist if the temperature was filtered similar to the strain rate. The hardness was significantly greater than the experimental hardness map. The only values that were relatively close were at the top of the hardness maps where the shoulder of the tool would pass. The inaccuracy of the empirical map was in large part due to the fact that none of the temperatures experienced in the FEM were in the temperature range that was derived for equation 3.12. This was evidenced by the fact that the equation is more accurate near the shoulder of the tool where the highest temperatures exist.

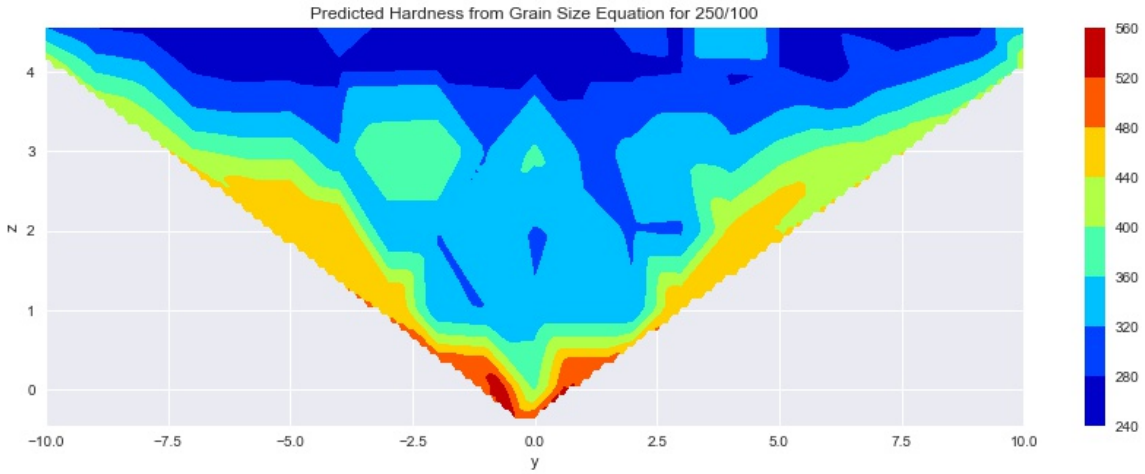

Figure 4.16: The empirical hardness derived from equations 3.12 and 3.13 for 250/100 parameter set. Values were filtered for those with strain rates greater than $0.1s^{-1}$.

To more thoroughly evaluate the random forest algorithm, new models were trained with slices of data across the z-axis held as the test data while the rest was used as the training data set. The new model was then used to predict the slices of data. Figure 4.17 displays the results with the R^2 measure in the subfigure descriptions.

Visually, the random forest predicted the 80/50 data very well with an R^2 value higher than 0.80 for four of the five. The model did not predict the 250/100 data set well relative to its performance on the 80/50 set. The model had lower accuracy in predicting the graphs that did not have a prominent increase in hardness in the welding zone. There was also a tendency for the random forest model to have sporadic behavior with extremely high or low predictions next to accurate predictions.

4.7 Discussion

Overall, the 250/100 data set was harder to predict in each step of evaluating the model. This was due to the lack of clear relationships between hardness and the independent variables. This can be seen in the scatterplot matrix for the 250/100 set (figure 4.10). Since there were no strong relationships, it was difficult for the model to effectively estimate the hardness relative to the 80/50 parameter set. This was an important finding because it highlights the importance of training the model with many different parameter sets in order to create a model that can predict other parameter sets.

One of the major drawbacks of using machine learning was that it can exhibit sporadic behavior by predicting extreme values in very smooth areas. A good example of this is in figure 4.17(e) at $y = 7.5$. There are a few points that have very high numbers relative to its predicted neighbors. As more data is added to the training data, this randomness would decrease and the model would be much more effective at having consistent predictions relative to a prediction's neighbors.

One question that cannot be answered in this thesis is if the random forest model is accurate because of the accuracy of the FEM or the random forest algorithm. The random forest algorithm effectively draws correlations between independent variables and dependent variables in such a way that even inaccurate data can be used to draw accurate conclusions. There is evidence that the temperature has moderate accuracy, however, it is still uncertain whether the strain rate has an acceptable level of accuracy.

While the FEM was tested and trained on the 250/100 data set, it seemed to be more accurate on the 80/50 data set. The quality of the data going into the random forest model from the FEM has a large impact on the accuracy of the final prediction. It is suspected that the reason the

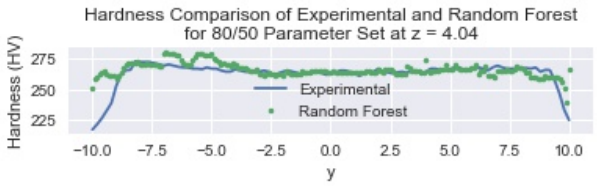

(a) $R^2 = 0.14$.

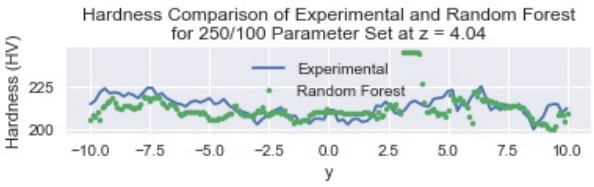

(b) $R^2 = -1.15$.

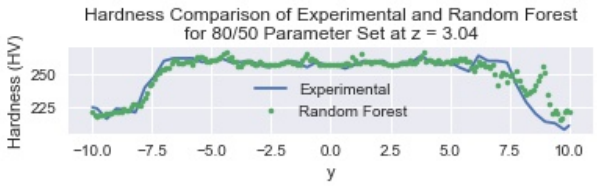

(c) $R^2 = 0.80$.

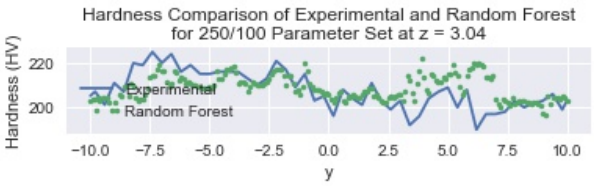

(d) $R^2 = -0.04$.

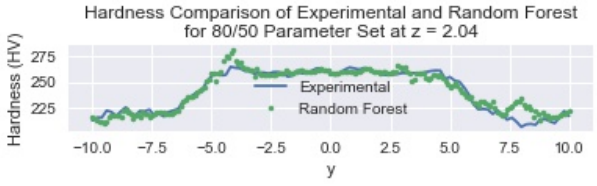

(e) $R^2 = 0.89$.

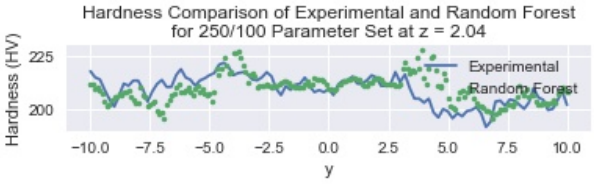

(f) $R^2 = -0.13$.

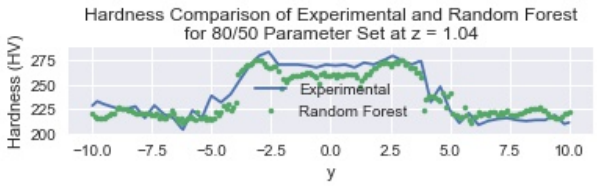

(g) $R^2 = 0.86$.

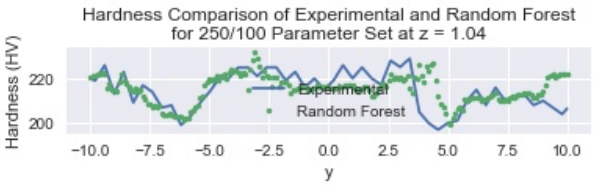

(h) $R^2 = 0.31$.

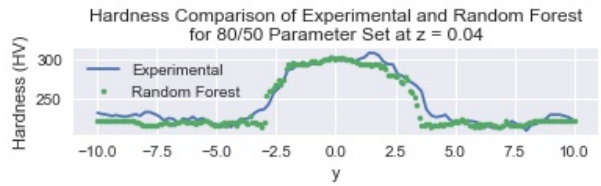

(i) $R^2 = 0.93$.

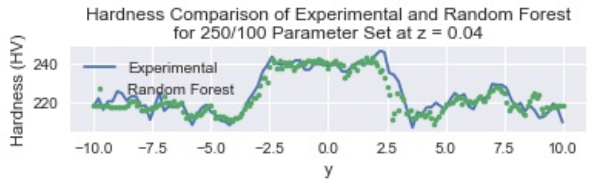

(j) $R^2 = 0.83$.

Figure 4.17: The hardness from experimental and random forest algorithm. The random forest algorithm was trained on all data except for the data in the individual graph. Each hardness graph holds z constant while letting y vary. The 80/50 set is on the left and the 250/100 set is on the right. The R^2 values are in the subfigure description.

full model predicted the 80/50 data set with such high accuracy relative to the 250/100 data set is because the FEM data is more accurate from the 80/50 FEM results than from the 250/100 FEM results. The 80/50 data set was never experimentally validated so it is uncertain whether it truly is more accurate.

CHAPTER 5. CONCLUSIONS

5.1 Conclusions

In this study, a FEM with an Eulerian formulation was constructed and analyzed for accuracy. A random forest algorithm was then trained and evaluated for accuracy. The following conclusions are made:

- The temperature and strain rate from the FEM was validated. The temperatures of the experimental and FEM were compared and were found to have high accuracy with a max error of 10.5%. The strain rate was validated through comparing the strain rate values of FSW in the literature. The strain rate in this FEM was found to agree with the values in the literature. Therefore, it is concluded that the temperature and strain rate is accurately predicted.

- The hardness for two parameter sets is predicted using temperature, cooling rate, strain rate, and RPM as independent variables. It was found that the random forest model accurately predicted the hardness maps with $R^2 = 0.95$.

- The random forest algorithm predicts the 80/50 parameter with much greater accuracy than the 250/100 parameter set. This highlights the importance of using different parameter sets to train the model.

5.2 Recommendations

There are two recommendations for future work that would further the work in this thesis.

- The model would be more effective as additional parameter sets are added to the model. Adding more parameter sets would be the first step to create a model that can be generalized to parameter sets that are not in the model training set.

- The quality of the weld was not addressed in this thesis. There are many welding parameters that result in inferior welds with defects such as pinholes. Creating another model that would predict the quality of the weld would greatly accelerate the ability to investigate possible FSW parameter sets.

REFERENCES

[1] Thomas, W., Nicholas, E., Needham, J., Murch, M., Templesmith, P., and Dawes, C., 1991. Great britain patent application no. 9125978.8. 1

[2] U.s. energy information administration - eia - independent statistics and analysis. 2

[3] Feng, Z., and Wilkowski, G., 2002. "Repair welding of irradiated materials: Modeling of helium bubble distributions for determining crack-free welding procedures." In *10th International Conference on Nuclear Engineering*, American Society of Mechanical Engineers, pp. 399–406. 2

[4] Yurioka, N., and Horii, Y., 2006. "Recent developments in repair welding technologies in japan." *Science and Technology of Welding and Joining,* **11**(3), pp. 255–264. 2

[5] Kanne, W., Chandler, G., Nelson, D., and Franco-Ferreira, E., 1995. "Welding irradiated stainless steel." *Journal of nuclear materials,* **225**, pp. 69–75. 2

[6] Gunter, C. C., 2016. "Feasibility of friction stir processing (fsp) as a method of healing cracks in irradiated 304l stainless steels.". 3, 19

[7] Moreno, D., Molina, B., Ranninger, C., Montero, F., and Izquierdo, J., 2004. "Microstructural characterization and pitting corrosion behavior of uns s30466 borated stainless steel." *Corrosion,* **60**(6), pp. 573–583. 5

[8] Wang, C., Grossbeck, M., Potluri, N., and Chin, B., 1996. "Welding of irradiated stainless steel." *Journal of nuclear materials,* **233**, pp. 213–217. 6

[9] Asano, K., Nishimura, S., Saito, Y., Sakamoto, H., Yamada, Y., Kato, T., and Hashimoto, T., 1999. "Weldability of neutron irradiated austenitic stainless steels." *Journal of Nuclear Materials,* **264**(1-2), pp. 1–9. 6

[10] Fraser, K., St-Georges, L., and Kiss, L. I., 2016. "A mesh-free solid-mechanics approach for simulating the friction stir-welding process.". 6

[11] Mahoney, M., and Lynch, S., 2006. Friction-stir processing Tech. rep., DTIC Document. 6, 7

[12] Benavides, S., Li, Y., Murr, L., Brown, D., and McClure, J., 1999. "Low-temperature friction-stir welding of 2024 aluminum." *Scripta materialia,* **41**(8), pp. 809–815. 6

[13] Rodriguez, N., Almanza, E., Alvarez, C., and Murr, L., 2005. "Study of friction stir welded a319 and a413 aluminum casting alloys." *Journal of materials science,* **40**(16), pp. 4307–4312. 6, 8

[14] Prado, R., Murr, L., Shindo, D., and Soto, K., 2001. "Tool wear in the friction-stir welding of aluminum alloy 6061+ 20% al 2 o 3: a preliminary study." *Scripta materialia,* **45**(1), pp. 75–80. 6, 8

[15] Mishra, R. S., Mahoney, M., McFadden, S., Mara, N., and Mukherjee, A., 1999. "High strain rate superplasticity in a friction stir processed 7075 al alloy." *Scripta Materialia,* **42**(2), pp. 163–168. 6, 7

[16] Li, Y., Murr, L., and McClure, J., 1999. "Flow visualization and residual microstructures associated with the friction-stir welding of 2024 aluminum to 6061 aluminum." *Materials Science and Engineering: A,* **271**(1), pp. 213–223. 6

[17] Jata, K., and Semiatin, S., 2000. Continuous dynamic recrystallization during friction stir welding of high strength aluminum alloys Tech. rep., Air force research lab wright-patterson afb oh materials and manufacturing . 6, 26

[18] Liu, F., and Nelson, T., 2017. "In-situ grain structure and texture evolution during friction stir welding of austenite stainless steel." *Materials & Design,* **115**, pp. 467–478. 6

[19] Cho, H.-H., Han, H. N., Hong, S.-T., Park, J.-H., Kwon, Y.-J., Kim, S.-H., and Steel, R. J., 2011. "Microstructural analysis of friction stir welded ferritic stainless steel." *Materials Science and Engineering: A,* **528**(6), pp. 2889–2894. 6, 8

[20] Sato, Y. S., Urata, M., Kokawa, H., Ikeda, K., and Enomoto, M., 2001. "Retention of fine grained microstructure of equal channel angular pressed aluminum alloy 1050 by friction stir welding." *Scripta Materialia,* **45**(1), pp. 109–114. 6

[21] Saeid, T., Abdollah-Zadeh, A., Assadi, H., and Ghaini, F. M., 2008. "Effect of friction stir welding speed on the microstructure and mechanical properties of a duplex stainless steel." *Materials Science and Engineering: A,* **496**(1), pp. 262–268. 6

[22] Mishra, R. S., and Mahoney, M. W., 2001. "Friction stir processing: a new grain refinement technique to achieve high strain rate superplasticity in commercial alloys." In *Materials Science Forum*, Vol. 357, Trans Tech Publ, pp. 507–514. 7

[23] Sorensen, C. D., and Nelson, T. W., 2007. "Friction stir welding of ferrous and nickel alloys." *Friction stir welding and processing*, pp. 111–121. 8

[24] Park, S. H. C., Sato, Y. S., Kokawa, H., Okamoto, K., Hirano, S., and Inagaki, M., 2003. "Rapid formation of the sigma phase in 304 stainless steel during friction stir welding." *Scripta Materialia,* **49**(12), pp. 1175–1180. 8

[25] Prado, R., Murr, L., Soto, K., and McClure, J., 2003. "Self-optimization in tool wear for friction-stir welding of al 6061+ 20% al 2 o 3 mmc." *Materials science and engineering: A,* **349**(1), pp. 156–165. 8

[26] Lee, W., Yeon, Y., and Jung, S., 2003. "Joint properties of friction stir welded az31b–h24 magnesium alloy." *Materials Science and Technology,* **19**(6), pp. 785–790. 8

[27] Nami, H., Adgi, H., Sharifitabar, M., and Shamabadi, H., 2011. "Microstructure and mechanical properties of friction stir welded al/mg 2 si metal matrix cast composite." *Materials & Design,* **32**(2), pp. 976–983. 8

[28] Collier, M., Steel, R., Nelson, T. W., Sorensen, C., and Packer, S., 2003. "Grade development of polycrystalline cubic boron nitride for friction stir processing of ferrous alloys." In *Materials Science Forum*, Vol. 426, Trans Tech Publ, pp. 3011–3016. 8

[29] Chowdhury, S., Chen, D., Bhole, S., and Cao, X., 2010. "Tensile properties of a friction stir welded magnesium alloy: Effect of pin tool thread orientation and weld pitch." *Materials Science and Engineering: A,* **527**(21), pp. 6064–6075. 8

[30] Kallee, S., 2010. "Industrial applications of friction stir welding." In *Friction stir welding*. Elsevier, pp. 118–163. 8, 9

[31] https://www2.mazda.com/en/publicity/release/2005/200506/050602.html, 2005. Mazda develops worlds first steel and aluminum joining technology using friction heat Publicity Release, June. 8

[32] Feng, Z., Santella, M., David, S., Steel, R., Packer, S., Pan, T., Kuo, M., and Bhatnagar, R., 2005. "Friction stir spot welding of advanced high-strength steels–a feasibility study." *SAE Transactions*, pp. 592–598. 8

[33] Sederstrom, J. H., 2007. "Spot friction welding of ultra high-strength automotive sheet steel.". 8

[34] Dudzik, K., and Czechowski, M., 2009. "Analysis of possible shipbuilding application of friction stir welding (fsw) method to joining elements made of alzn5mg1 alloy." *Polish Maritime Research,* **16**(4), pp. 38–40. 9

[35] Källgren, T., 2005. "Friction stir welding of copper canisters for nuclear waste." PhD thesis, KTH. 9

[36] Guerdoux, S., Fourment, L., Miles, M., and Sorensen, C., 2004. "Numerical simulation of the friction stir welding process using both lagrangian and arbitrary lagrangian eulerian formulations." In *AIP Conference Proceedings*, Vol. 712, AIP, pp. 1259–1264. 9, 10

[37] Al-Badour, F., Merah, N., Shuaib, A., and Bazoune, A., 2013. "Coupled eulerian lagrangian finite element modeling of friction stir welding processes." *Journal of Materials Processing Technology,* **213**(8), pp. 1433–1439. 10

[38] Assidi, M., Fourment, L., Guerdoux, S., and Nelson, T., 2010. "Friction model for friction stir welding process simulation: Calibrations from welding experiments." *International Journal of Machine Tools and Manufacture,* **50**(2), pp. 143–155. 10

[39] Zhang, H., Zhang, Z., and Chen, J., 2007. "3d modeling of material flow in friction stir welding under different process parameters." *Journal of Materials Processing Technology,* **183**(1), pp. 62–70. 10

[40] Miles, M., Nelson, T., Gunter, C., Liu, F., Fourment, L., and Mathis, T., 2019. "Predicting recrystallized grain size in friction stir processed 304l stainless steel." *Journal of materials science & technology,* **35**(4), pp. 491–498. 10

[41] Buffa, G., Fratini, L., and Shivpuri, R., 2007. "Cdrx modelling in friction stir welding of aa7075-t6 aluminum alloy: Analytical approaches." *Journal of Materials Processing Technology,* **191**(1-3), pp. 356–359. 10

[42] Fratini, L., Buffa, G., and Palmeri, D., 2009. "Using a neural network for predicting the average grain size in friction stir welding processes." *Computers & Structures,* **87**(17-18), pp. 1166–1174. 10, 12

[43] Saluja, R. S., Narayanan, R. G., and Das, S., 2012. "Cellular automata finite element (cafe) model to predict the forming of friction stir welded blanks." *Computational Materials Science,* **58**, pp. 87–100. 10

[44] Colegrove, P. A., and Shercliff, H. R., 2005. "3-dimensional cfd modelling of flow round a threaded friction stir welding tool profile." *Journal of materials processing technology,* **169**(2), pp. 320–327. 10, 26

[45] Colegrove, P., and Shercliff, H., 2006. "Cfd modelling of friction stir welding of thick plate 7449 aluminium alloy." *Science and Technology of welding and joining,* **11**(4), pp. 429–441. 10

[46] Chen, G.-q., Shi, Q.-y., Li, Y.-j., Sun, Y.-j., Dai, Q.-l., Jia, J.-y., Zhu, Y.-c., and Wu, J.-j., 2013. "Computational fluid dynamics studies on heat generation during friction stir welding of aluminum alloy." *Computational Materials Science,* **79**, pp. 540–546. 10

[47] Long, T., and Reynolds, A. P., 2006. "Parametric studies of friction stir welding by commercial fluid dynamics simulation." *Science and Technology of Welding and Joining,* **11**(2), pp. 200–208. 10

[48] Colegrove, P., and Shercliff, H., 2004. "Development of trivex friction stir welding tool part 2–three-dimensional flow modelling." *Science and Technology of Welding and Joining,* **9**(4), pp. 352–361. 10

[49] Song, M., and Kovacevic, R., 2003. "Thermal modeling of friction stir welding in a moving coordinate system and its validation." *International Journal of machine tools and manufacture,* **43**(6), pp. 605–615. 11

[50] Schmidt, H., Hattel, J., and Wert, J., 2003. "An analytical model for the heat generation in friction stir welding." *Modelling and Simulation in Materials Science and Engineering,* **12**(1), p. 143. 11

[51] Venugopal, S., and Sivaprasad, P., 2003. "A journey with prasads processing maps." *Journal of materials engineering and performance,* **12**(6), pp. 674–686. 11, 19

[52] Tansel, I. N., Demetgul, M., Okuyucu, H., and Yapici, A., 2010. "Optimizations of friction stir welding of aluminum alloy by using genetically optimized neural network." *The International Journal of Advanced Manufacturing Technology,* **48**(1-4), pp. 95–101. 12

[53] Boldsaikhan, E., Corwin, E. M., Logar, A. M., and Arbegast, W. J., 2011. "The use of neural network and discrete fourier transform for real-time evaluation of friction stir welding." *Applied Soft Computing,* **11**(8), pp. 4839–4846. 12

[54] Okuyucu, H., Kurt, A., and Arcaklioglu, E., 2007. "Artificial neural network application to the friction stir welding of aluminum plates." *Materials & design,* **28**(1), pp. 78–84. 12

[55] https://elitedatascience.com/algorithm selection, 2018. Algorithm selection. 13

[56] Sabooni, S., Karimzadeh, F., Enayati, M., Ngan, A., and Jabbari, H., 2015. "Gas tungsten arc welding and friction stir welding of ultrafine grained aisi 304l stainless steel: microstructural and mechanical behavior characterization." *Materials Characterization,* **109**, pp. 138–151. 26

[57] Masaki, K., Sato, Y. S., Maeda, M., and Kokawa, H., 2008. "Experimental simulation of recrystallized microstructure in friction stir welded al alloy using a plane-strain compression test." *Scripta Materialia,* **58**(5), pp. 355–360. 26

[58] Frigaard, Ø., Grong, Ø., and Midling, O., 2001. "A process model for friction stir welding of age hardening aluminum alloys." *Metallurgical and materials transactions A,* **32**(5), pp. 1189–1200. 26